Article

Electrically driven long-range solid-state amorphization in ferroic In_2Se_3

https://doi.org/10.1038/s41586-024-08156-8

Received: 11 July 2023

Accepted: 4 October 2024

Published online: 06 November 2024

Check for updates

Gaurav Modi[1,4], Shubham K. Parate[2,4], Choah Kwon[3], Andrew C. Meng[1], Utkarsh Khandelwal[1], Anudeep Tullibilli[2], James Horwath[1], Peter K. Davies[1], Eric A. Stach[1], Ju Li[3], Pavan Nukala[2]✉ & Ritesh Agarwal[1]✉

Electrically induced amorphization is uncommon and has so far been realized by pulsed electrical current in only a few material systems, which are mostly based on the melt–quench process[1]. However, if the melting step can be avoided and solid-state amorphization can be realized electrically, it opens up the possibility for low-power device applications[2–5]. Here we report an energy-efficient, unconventional long-range solid-state amorphization in a new ferroic β″-phase of indium selenide nanowires through the application of a direct-current bias rather than a pulsed electrical stimulus. The complex interplay of the applied electric field perpendicular to the polarization, current flow parallel to the van der Waals layer and piezoelectric stress results in the formation of interlayer sliding defects and coupled disorder induced by in-plane polarization rotation in this layered material. On reaching a critical limit of the electrically induced disorder, the structure becomes frustrated and locally collapses into an amorphous phase[6], and this phenomenon is replicated over a much larger microscopic-length scale through acoustic jerks[7,8]. Our work uncovers previously unknown multimodal coupling mechanisms of the ferroic order in materials to the externally applied electric field, current and internally generated stress, and can be useful to design new materials and devices for low-power electronic and photonic applications.

The microscopic mechanisms driving the formation of amorphous and other disordered phases from ordered phases in materials has long perplexed scientists[9–11]. Conventionally, amorphization involves the rapid cooling of a liquid melt, bypassing thermodynamically favourable crystallization[12]. However, direct crystal–amorphous transformation without going through a melt–quench process are also known[13]. Examples of solid-state amorphization (SSA) pathways include ion irradiation[14], high-pressure treatment[15] and severe plastic deformation[16]. SSA proceeds by the addition of defects to a crystal, thereby creating a metastable crystalline phase. When disorder reaches a threshold, the crystalline phase becomes unstable and it collapses into an amorphous phase[2,6]. Although there are a few examples of amorphization in which a mechanically driven process is used, electrically driven SSA is relatively uncommon and discovering their pathways in new materials will be useful for designing energy-efficient devices[3,4].

Electrically driven SSA was reported in single-crystalline nanowires of phase-change-memory germanium–antimony–tellurium (Ge–Sb–Te) alloys in which an interplay of unique bonding hierarchy, structural distortion and large number of Ge vacancies resulted in defect-mediated amorphization[2,3]. In crystalline GeTe, polar ordering was observed. However, degenerate doping from Ge vacancies renders the system metallic, which precludes the direct coupling of polar domains with an external electric field[17–19]. Thus, in Ge–Sb–Te, carrier wind force interaction with defects and polar domains was used to construct a low-power SSA pathway. Conventional ferroelectrics are electrically insulating[20], which allows the order parameter to couple with the electric field and not with the carrier wind force. Using field-controlled frustration and disorder in ferroic systems to design low-energy SSA is an unexplored territory and requires finding materials with the right balance of ferroic nature and electrical conductivity to enable a multimode coupling to electric field and current. Polymorphs of indium selenide (In_2Se_3) provide rare materials platforms that can be both ferroic and semiconducting[21–24]. Here we explore the unusual coupling between the electric field, current, ensuing stress and structural order in a new ferroelectric β″-phase of In_2Se_3 nanowires and illustrate how it leads to an unconventional crystal–amorphous transformation. We show that the electric field and current create interlayer-sliding-induced faults and coupled in-plane polarization rotation, eventually leading to a frustrated multiconfigurational state, which is a precursor for local (nanoscopic) SSA. This process is spatially replicated over a much larger microscopic-length scale through piezoelectric stress and stress fluctuations, resulting in long-range amorphization. Our experiments shed light on the mechanisms behind a fundamentally different order–disorder transition through a multimodal coupling between ferroic and crystalline order with an external field, current and piezoelectric stress.

[1]Department of Materials Science and Engineering, University of Pennsylvania, Philadelphia, PA, USA. [2]Centre for Nanoscience and Engineering, Indian Institute of Science, Bengaluru, India. [3]Department of Materials Science and Engineering, Massachusetts Institute of Technology, Cambridge, MA, USA. [4]These authors contributed equally: Gaurav Modi, Shubham K. Parate. ✉e-mail: pnukala@iisc.ac.in; riteshag@seas.upenn.edu

Crystal structure and ferroelectricity in β″-In_2Se_3

In_2Se_3 has many polymorphs such as α, β, β′, γ, δ and κ (ref. 25), with many of them having ferroic properties. β′-In_2Se_3 is particularly interesting as it has been reported to be antiferroelectric[23], ferrielectric[26] and ferroelastic[24]. We synthesized In_2Se_3 nanowires in a new ferroelectric variant of the β′-phase (which we refer to as β″-In_2Se_3) through a catalyst-assisted vapour–liquid–solid growth mechanism[27] (Methods and Supplementary Fig. 1). The crystal structure of the as-synthesized nanowires was characterized by scanning transmission electron microscopy (STEM). Selected area electron diffraction (SAED) data show that the nanowires are single crystalline with a <11$\bar{2}$0> growth direction (Fig. 1a). In addition to the primary SAED reflections for a rhombohedral crystal, three discernible superlattice reflections along <1$\bar{1}$00> can also be seen, suggesting a superstructure formation (Supplementary Fig. 2 shows the simulated SAED) with a periodicity of $4d_{1\bar{1}00}$ (ref. 27). This is in contrast to the 7–9 superlattice reflections reported for β′-In_2Se_3 (ref. 23). Hence, depending on the nanomaterial shape and geometry, the ferroic order in β′-In_2Se_3 variants can have multiple possible configurations and many metastable states (Supplementary Note 1). High-resolution (HR) high-angle annular dark-field (HAADF) STEM imaging further shows the bright–dark contrast modulation due to superstructure formation with approximately 1.35 nm ($4d_{1\bar{1}00}$) periodicity along <1$\bar{1}$00> (Fig. 1b,e). Notably, the contrast from the lattice sites in our HRSTEM images is inverted compared with 2H β′-In_2Se_3 (refs. 23,24,26), which suggests a stacking variant of type 1T (ref. 28) (Supplementary Figs. 3 and 4). The 1T phase is rare in In_2Se_3 and has been reported only in nanowires[28]. Fast Fourier transform (FFT) of the HRSTEM image (Fig. 1b, inset) also shows three superlattice reflections. However, in some regions, extra weak spots and diffuse streaking are also observed due to some defects (dislocations) in the pristine nanowire (Supplementary Fig. 5). The atomic displacement map (Fig. 1c), in which we track the in-plane geometrical displacement of the central Se atom (darker contrast) relative to the brighter hexagonal reference lattice sites, shows that, on average, the in-plane Se displacement is approximately 15 pm and along <1$\bar{1}$00>, as opposed to the antiferroelectric or ferrielectric arrangement with polarization along <11$\bar{2}$0> in β′-In_2Se_3. Crystal symmetry analysis by convergent-beam electron diffraction shows a {11$\bar{2}$0} mirror plane (Fig. 1d and Supplementary Fig. 6) for β″-In_2Se_3 nanowires in contrast to a {1$\bar{1}$00} mirror plane for β′-In_2Se_3 (ref. 23).

Energy-dispersive X-ray spectroscopy (EDX) mapping (Fig. 1g and Supplementary Fig. 7) shows a periodic oscillation of the In/Se ratio, which we attribute to periodic In- and Se-vacancy-rich layers. The dark bands in the superstructure correspond to In-vacancy-rich regions, whereas Se-vacancy-rich regions correspond to the centre of the brighter bands, which is further confirmed by the line intensity profile of the HRSTEM image (Fig. 1e). The ordering of In vacancies has also been reported for other In-based chalcogenides such as β-In_2S_3 (refs. 29,30). Assuming nominal positive and negative charges for the Se and In vacancies, respectively, the periodically alternating vacancy-rich layers overlay an extra polarization order on the ferroelectric polarization due to Se displacements, leading to an overall ferroelectric order (Fig. 1f and Supplementary Fig. 8). Piezoresponse force microscopy (PFM) shows an off-field butterfly amplitude response[31], and a 180° phase flip (Supplementary Fig. 9), suggesting polarization switching, consistent with the presence of spontaneous ferroelectric polarization perpendicular to the growth axis (<11$\bar{2}$0>). Our DFT calculations (Methods) also validate the stability of the experimentally observed crystal structure of β″-In_2Se_3 (Fig. 1h, Supplementary Fig. 10 and Supplementary Note 2).

TEM observation of amorphization by d.c. bias

To understand the evolution of the microstructure and its relationship to its peculiar ferroelectric order on applying external electric fields, we fabricated In_2Se_3 nanowire transmission electron microscopy (TEM) devices (Methods and Supplementary Fig. 11). TEM characterization of the pristine nanowire device confirms that it has the same structure as discussed above (Fig. 2a,b). We applied direct current (d.c.) current–voltage (I–V) sweeps to this device (Fig. 2c), in which the compliance current (I_c) was slightly increased after each sweep. No changes in device resistance were observed for the first three I–V sweeps (I_c = 3.0 μA for the third sweep), but for the fourth sweep (I_c = 3.5 μA), we observed a sudden drop in current from approximately 3.1 μA to around 0.09 μA. To understand the origin of the increase in device resistance, we performed TEM imaging in which the low-magnification bright-field TEM image (Fig. 2d) clearly shows no breakage or large voids. Dark-field (DF) TEM (Fig. 2h) and HRTEM imaging (Fig. 2k) surprisingly showed that almost the entire nanowire section suspended over the trench had amorphized, accompanied by a diffuse halo contrast in the SAED data (Fig. 2e). We emphasize that the amorphization of In_2Se_3 occurred under a d.c. bias, which is different from the pulsed current required to amorphize Ge–Sb–Te nanowires[2]. Moreover, the amorphous section in the β″-In_2Se_3 nanowire spanned a large lateral width of >1 μm with a clear crystal–amorphous interface (Fig. 2h–j, blue box), and the untransformed crystalline region (Fig. 2h, green arrows) remained single crystalline and retained its superstructure (Fig. 2g,l). This is in contrast to the amorphous region with a typical width of only approximately 20 nm surrounded by a highly defective but crystalline region in Ge–Sb–Te nanowires[2,3,18,32,33]. Hence, we refer to such a crystal–amorphous transformation as 'unconventional'. EDX mapping of In/Se did not indicate any measurable differences in the stoichiometry between the crystalline and amorphous regions and as-grown nanowires (Fig. 2m and Supplementary Fig. 12), suggesting a polymorphous transition[34]. Finite-element simulations (Supplementary Fig. 13) indicate a temperature of approximately 410 K for the d.c.-biased nanowire, much less than the melting temperature of In_2Se_3 (1,163 K), ruling out the possibility of melting before amorphization (Supplementary Notes 3 and 4). Furthermore, in another device, amorphization occurred with a delay of approximately 6.2 s after applying a bias of 20 V (Extended Data Fig. 1), which reaffirms that heating (temperature) is not the sole driving force for amorphization, and a critical density of defects must be accumulated before amorphization can occur (discussed later).

Structure evolution along the amorphization pathway

Next, we applied multiple stepwise d.c. I–V sweeps (Fig. 3a) to another nanowire device to observe the structural changes occurring along the amorphization pathway. We observed that at higher voltages (>11.5 V), the I–V curve became noisy followed by a negative differential resistance (NDR) region at V > 12.75 V, followed by a permanent reduction in conductivity (Fig. 3a and Supplementary Fig. 14), suggesting the origin to be structural as opposed to electronic (Supplementary Note 5). TEM characterization of the device following NDR indeed showed evidence of numerous sliding faults, but the nanowire was still crystalline. After biasing at a d.c. electric field of approximately 10–50 kV cm^{-1} (15 V) and current density of around 10^{-2}–10^{-1} MA cm^{-2} (6–8 μA), the SAED (Fig. 3b) data show diffuse diffraction spots, along with the emergence of forbidden reflections, implying the presence of many structural imperfections (Supplementary Fig. 5). DFTEM images show unusual contrast modulations throughout the nanowire (Supplementary Fig. 15 and Fig. 3c) and that the bright–dark superstructure stripes, which were initially completely parallel along the long axis of the pristine nanowire, were distorted after electrical biasing. Application of further d.c. I–V sweeps to this nanowire resulted in sudden amorphization (Supplementary Fig. 16), suggesting its direct relationship with the observed structural changes (discussed in detail later).

HR HAADF-STEM images of another d.c.-biased nanowire device (Fig. 3d,e) further confirm this distortion, which arises because of

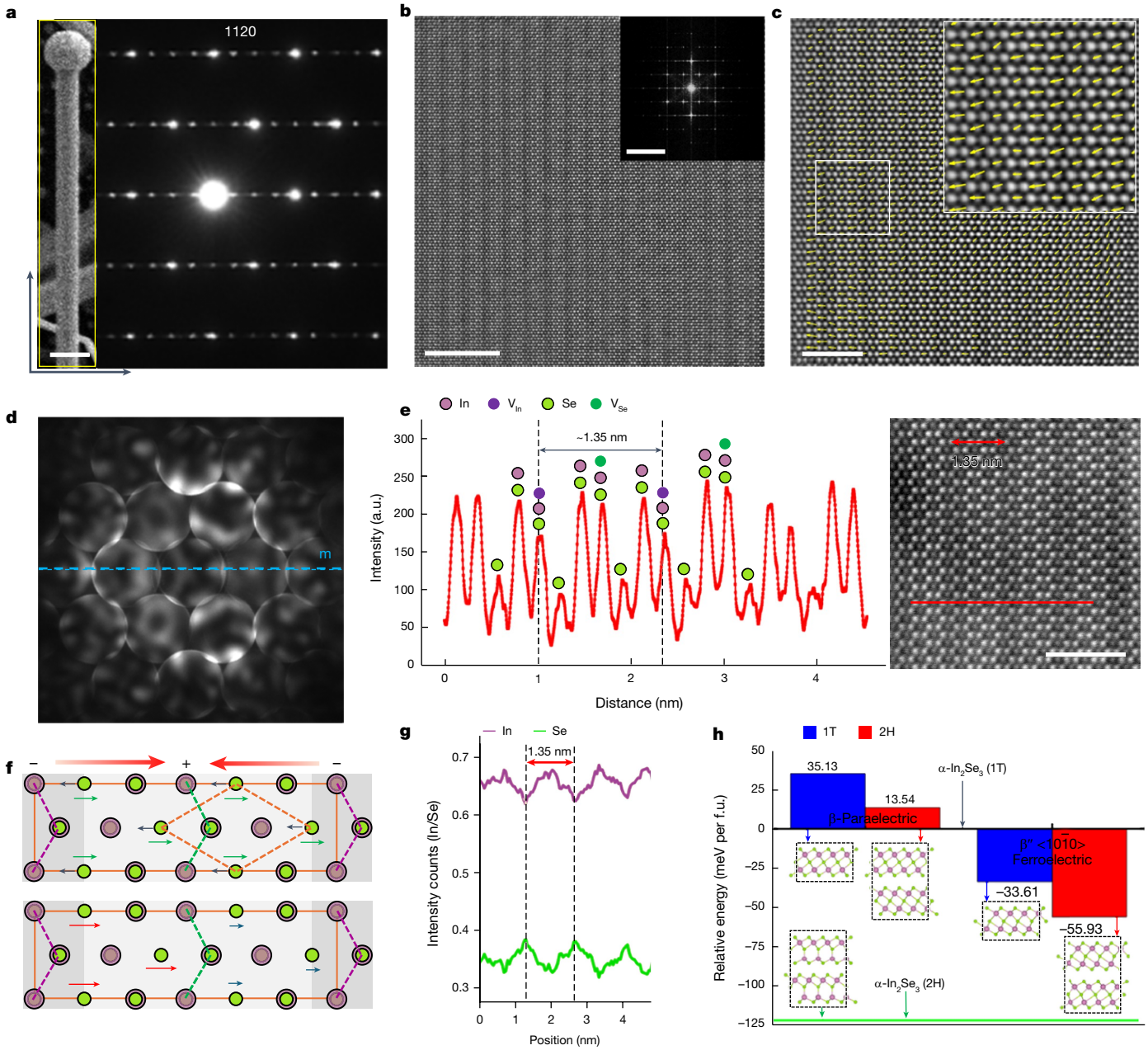

Fig. 1 | TEM characterization of as-synthesized β″-In_2Se_3 nanowires. a, Electron diffraction along the <0001> zone axis showing the presence of three superlattice reflections along one of the <1$\bar{1}$00> directions. The inset shows the scanning electron microscopy image of an In_2Se_3 nanowire with a Au–Pd catalyst at the tip. **b**, HAADF-STEM image showing superstructure modulation along <1$\bar{1}$00>. The inset shows the FFT of the STEM image. **c**, Se-atom displacement map showing that, on average, Se displacement is along <1$\bar{1}$00>, resulting in net polarization along that direction. The inset shows the magnified map of the region indicated by the white box. **d**, Convergent-beam electron diffraction data of the as-synthesized β″-In_2Se_3 nanowire, showing the presence of a {11$\bar{2}$0} mirror plane. **e**, Line intensity profile mapping along <1$\bar{1}$00> from the region indicated by the red line in the HAADF-STEM image in the inset. It reveals a 1T-stacking variant and the periodic dark regions are due to the presence of ordered In vacancies (V_{In}). V_{Se}, Se vacancies; a.u., arbitrary units. **f**, Schematic of the proposed crystal structure when viewed along <0001>, where the purple and green spheres represent the In and Se atoms, respectively. Se displacement is shown by the black arrows and polarizations are shown by the coloured arrows. The orange box indicates the unit cell of the β″-In_2Se_3 phase and the dashed orange rhombus indicates the unit cell of paraelectric β-In_2Se_3 with no Se displacements. The dashed purple and green lines pass through the lattice sites rich in In and Se vacancies, respectively. The schematic at the bottom indicates the final ferroelectric polarization arrangement due to the superposition of polarizations from vacancy layers and those due to Se displacement. **g**, EDX line profile showing the periodic variation in In and Se compositions along <1$\bar{1}$00>, implying the presence of periodic In- and Se-vacancy-rich layers. **h**, DFT calculations of the relative energies of various polymorphs of In_2Se_3 along with the schematic for the crystal structures. f.u., formula unit. Scale bars, 5 nm (**b**), 2 nm (**c** and **e**) and 10 nm^{-1} (**b**, inset).

field/current-induced interlayer sliding and the corresponding sliding faults[35]. In the next stage, at larger bias voltages (approximately 0.1 MA cm^{-2}), in which current exhibits fluctuations, eventually decreasing with increasing voltage (NDR), several sliding faults interact with each other, creating nanoscopic domains (Fig. 3f). Some of these domains can be simulated as overlapping crystals (along the $\vec{c}$ axis), with one part of the crystal sliding relative to another by different lattice and sub-lattice vectors (Fig. 3h,i and Supplementary Notes 6–8). Our calculations show that the activation barrier for nucleating one nanoscopic domain D2 by interlayer sliding is only

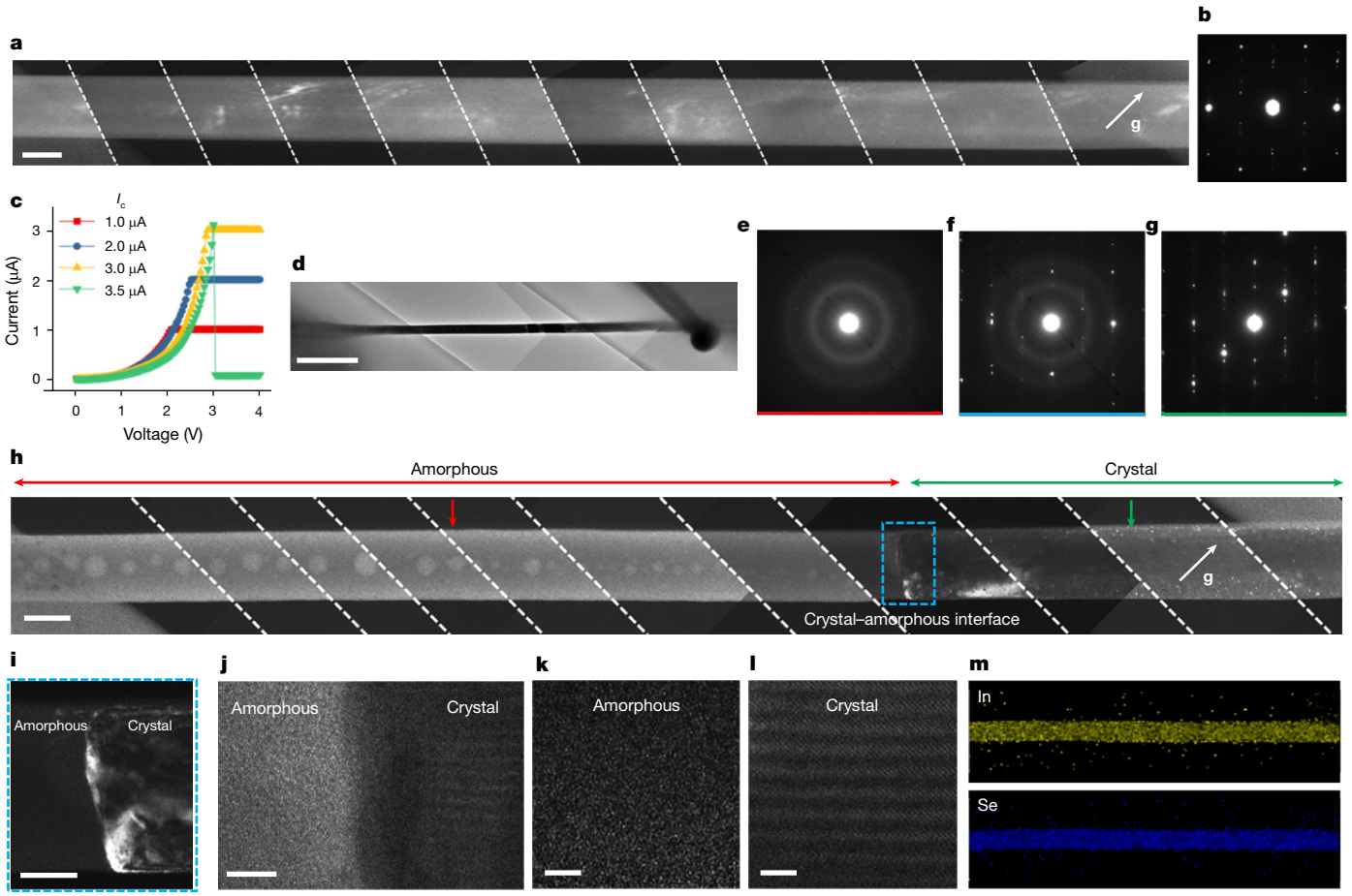

Fig. 2 | Amorphization induced by a d.c. voltage in a β″-In_2Se_3 nanowire device. a,**b**, DFTEM image (**a**) and SAED data (**b**) of a pristine nanowire device before applying any electrical stimuli. **g** indicates the reciprocal lattice vector used for DFTEM imaging. **c**, Series of 0–4 V d.c. *I*–*V* sweeps applied to the nanowires in which the compliance current was gradually increased. A sudden drop in current is seen when the current reaches approximately 3.1 μA, indicating possible amorphization. **d**, Low-magnification TEM image of the nanowire after amorphization, confirming that the drop in current was not because of breaking of the nanowire but due to amorphization. **e**–**g**, SAED data of the nanowire from the amorphous region (**e**), crystal–amorphous interface (**f**) and crystalline region (**g**) as indicated in the DFTEM image. **h**, DFTEM image of the nanowire in which the crystal–amorphous interface is indicated by the blue dashed box. The entire left side of the nanowire suspended over the trench became amorphous. Owing to the difference in material density between the amorphous and crystalline phases and a large volume of nanowire undergoing amorphization in a rather uncontrolled manner, some nanoscale voids were observed in the amorphized region. **i**,**j**, Crystal–amorphous interface is further shown in the DFTEM image (**i**) and HRTEM image (**j**). **k**,**l**, HRTEM image from the amorphous (**k**) and crystalline (**l**) regions of the nanowire. **m**, EDX mapping of the nanowires for the elements In and Se after amorphization. The dashed white lines in **a** and **h** indicate the regions in which the images were combined. Scale bars, 100 nm (**a** and **h**), 1 μm (**d**), 50 nm (**i**), 5 nm (**j**), 2 nm (**k** and **l**).

149.1 meV (Fig. 3g,h). Hence, several such nanoscopic configurations can be created with small driving forces, resulting in a free-energy landscape with multiple local minima along the reaction coordinate (Supplementary Fig. 17a). Such a high-entropy configuration is a precursor for localized SSA, as can be noted from the DFTEM image and corresponding FFT acquired from the region of intersecting defects (Fig. 4a–c).

Furthermore, spontaneous polarization will also respond to the electric field[36], positively feeding back into the creation of sliding faults through the carrier wind force. Hence, the initial <1$\bar{1}$00> polarization direction, which is a metastable phase in β″-In_2Se_3 nanowires formed during growth, can easily rotate its polarization orthogonally under the application of a d.c. bias (Fig. 3g). However, the polarization rotation is not homogeneous due to pre-existing and electrically generated inhomogeneities and defects, generating inhomogeneous piezoelectric stress[37,38]. Along with Joule-heating-assisted dipole disordering, these factors create a 'frustrated' multidomain polarization state. This state is visible from the streaky position of Se atoms in the HRSTEM image (Fig. 3e,f), with each polarization domain intertwined with the nanoscopic stacking domains (Fig. 3f).

In situ TEM observation of amorphization

To visualize the real-time microstructural evolution leading to long-range SSA because of multimodal coupling (field, stress, current and temperature), we performed in situ biasing on another device with some prior electrical history (Supplementary Fig. 18 and Supplementary Note 9) and followed its time evolution through DFTEM imaging (Fig. 4a; resolution approximately, 1 nm; **g** = [1$\bar{1}$00]) and the corresponding FFT. The FFT in the starting state captures superstructure reflections (Fig. 4b), which will be interpreted as a proxy for long-range structural order. The DFTEM image shows sliding faults (and other disorder) appearing as a diffuse halo in the FFT (Fig. 4b) with applied bias. Regions in which several faults intersect do not show any long-range order (Fig. 4c,d), indicating a localized 'nucleation' of SSA.

Supplementary Video 1 shows that small bias voltages (approximately 5 V) also create subtle dynamics to the already existing sliding defects, as can also be noted from the series of FFTs at different times (Supplementary Fig. 18). Supplementary Video 2 shows the defect dynamics on subjecting the device to *I*–*V* stressing from 15 to 25 V. In the transport behaviour, we observe current fluctuations at a bias of >20 V (Fig. 4e),

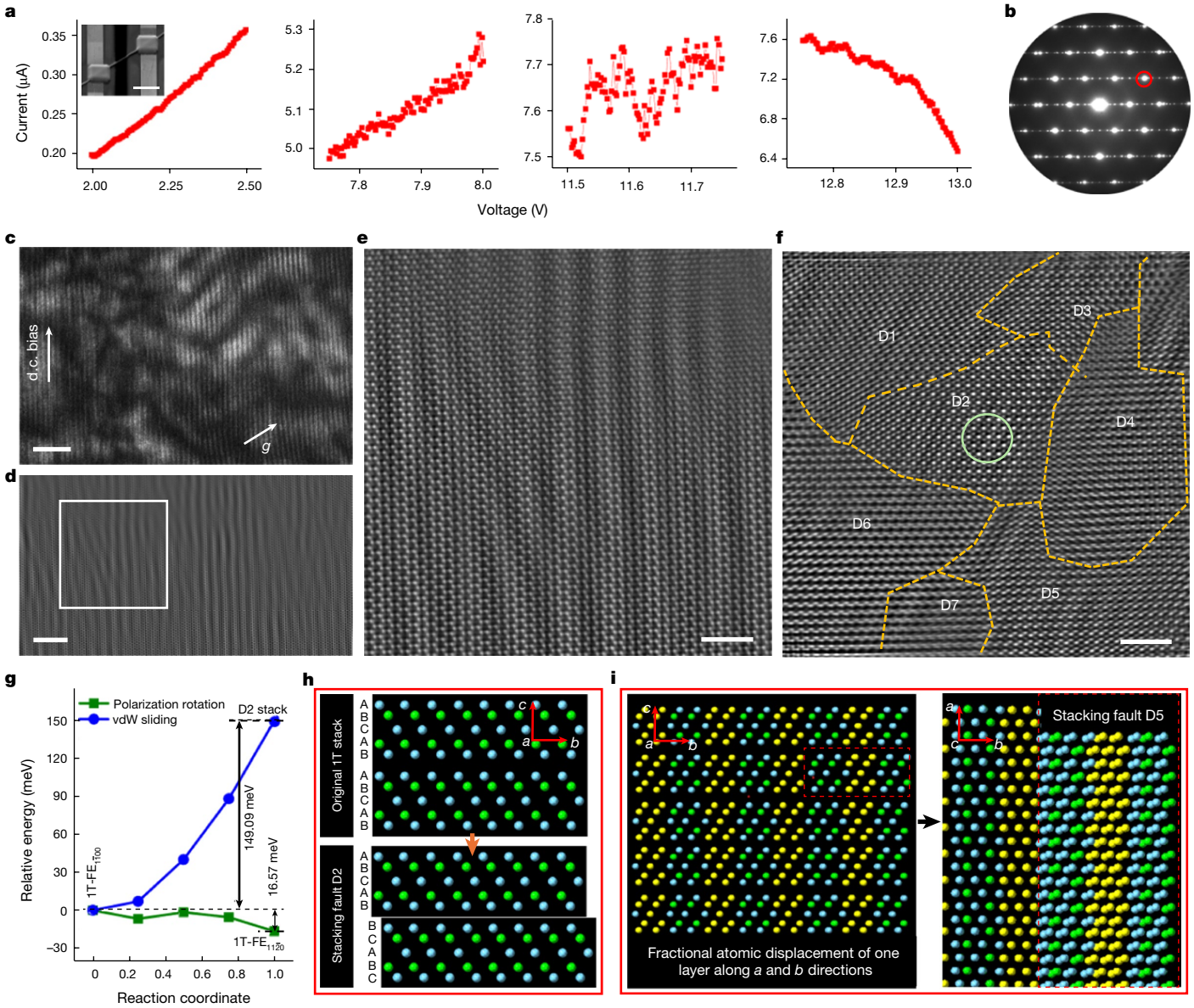

Fig. 3 | STEM analysis of a β″-In_2Se_3 nanowire device exhibiting sliding faults after applying a series of d.c. *I*–*V* sweeps before amorphization. a, *I*–*V* sweeps on the nanowire showing a change in behaviour from a positive *I*–*V* slope to noisy behaviour and finally the slope becoming negative, indicating an increase in structural disorder (the nanowire is still crystalline). The inset shows the scanning electron microscopy image of a nanowire device on a TEM chip. Scale bar, 5 μm. **b**, Electron diffraction showing the appearance of extra superlattice reflections apart from the usual three, which indicates the formation of numerous lattice defects in the nanowire. The red circled spot was used for DFTEM imaging. **c**–**e**, DFTEM (**c**), low-magnification HRSTEM (**d**) and high-magnification HRSTEM (**e**) images from a different nanowire device after multiple *I*–*V* sweeps, showing the distortion of the superstructure because of the creation of sliding faults. The superstructure contrast is enhanced first by Bragg filtering the raw HRSTEM image (Supplementary Fig. 19c) and then overlaying it on the Fourier-filtered image showing just the superstructure periodicity (Supplementary Fig. 19e). **f**, HAADF-HRSTEM image showing various nanoscopic regions (indicated by D1, D2, D3 and so on) created by interlayer-sliding-induced disorder just before amorphization. **g**, DFT-trained machine learning calculation of the activation barrier for the rotation of polarization from the <1$\bar{1}$00> to <11$\bar{2}$0> direction and for interlayer sliding along <1$\bar{1}$00>. **h**, Schematic of transformation from 1T (ABCAB ABCAB) to D2 (ABCAB BCABC) configuration through interlayer van der Waals (vdW) sliding mechanism. **i**, Results from the simulation on the steps involved in forming the nanoscopic region with stacking configuration D5. Scale bars, 10 nm (**c**), 5 nm (**d**), 2 nm (**e**) and 2 nm (**f**).

similar to other devices (Fig. 3a and Supplementary Figs. 14 and 22a). The DFTEM video shows that concomitant with the current fluctuations (or local field fluctuations), the strain field also fluctuates in a correlated manner (snapshots in Fig. 4f–h) obtained at the corresponding points (labelled f, g and h) on the *I*–*t* curve (Fig. 4e). The perfect synchronization of field fluctuations (Fig. 4e) and acoustic jerks (Fig. 4f–h) is evidence of piezoelectricity, and these jerks themselves resemble Barkhausen noise characteristic of disordered ferroelectrics emanating from intersecting dynamic domain boundaries[7,8,39]. Conversely, the observation of such noise stands as the evidence of polarization rotation and interaction among sliding faults and domains in our system[40] (Supplementary Note 9).

Supplementary Video 3 captures the amorphization process, which immediately follows the current fluctuations and the NDR regime (Fig. 4i). On following the FFT of the DFTEM image, we see that the FFT, to start with, shows streaky patterns (Fig. 4j) of what were sharper modulation vectors (Fig. 4b), clearly suggesting an increase in disorder in the superstructure arising from In- and Se-vacancy ordering,

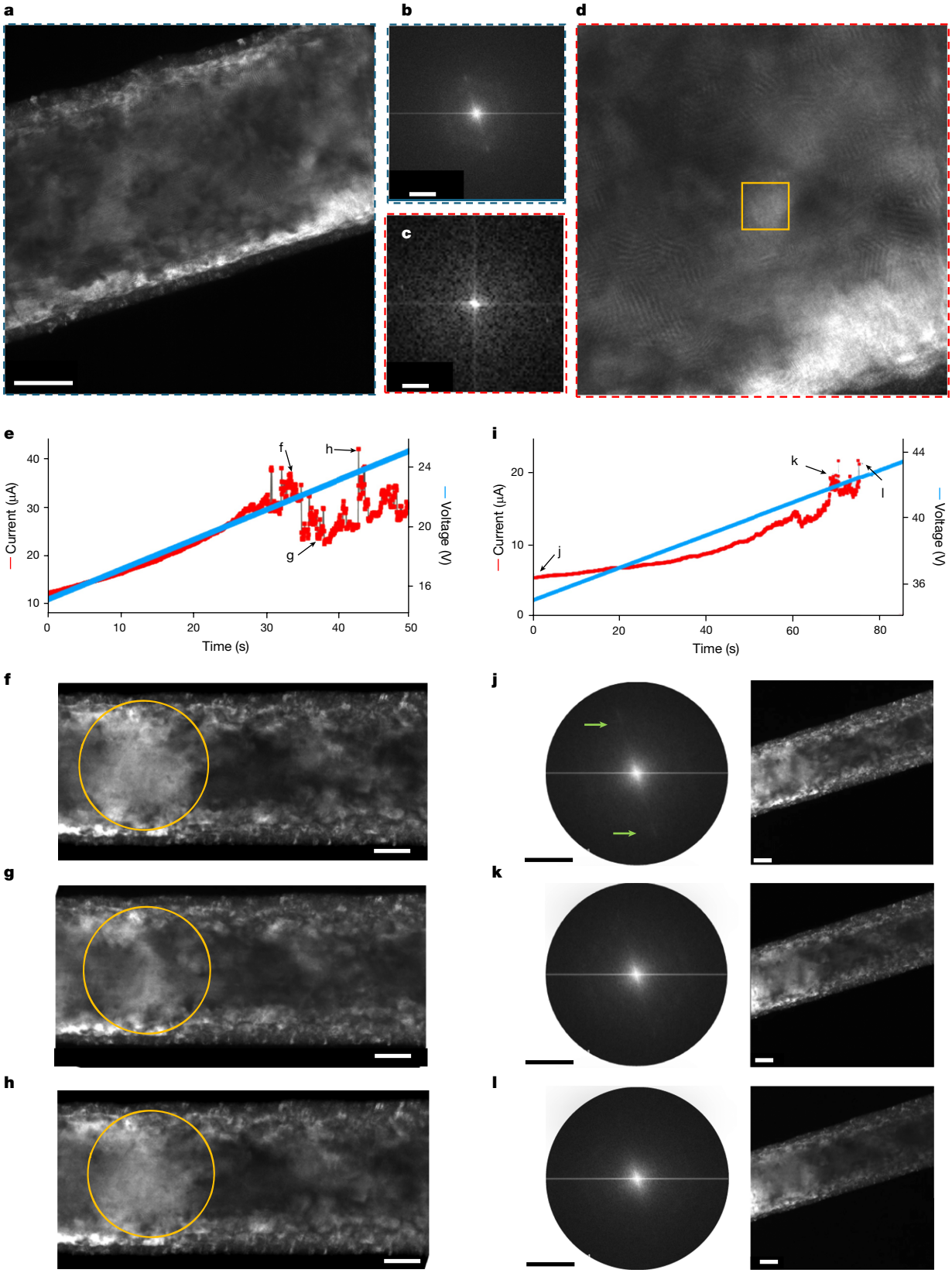

Fig. 4 | In situ biasing DFTEM imaging of β″-In_2Se_3 nanowire device and observation of amorphization. a,**b**, DFTEM image of the initial state of another nanowire device (**a**) and the corresponding FFT (**b**) showing superstructure reflections and a diffuse halo corresponding to sliding faults and other defects or disorder. **c**,**d**, FFT (**c**) of a region obtained from the intersection of several sliding faults marked in the DFTEM image in **d**, showing a local loss of order. **e**–**h**, *V*–*t* and *I*–*t* characteristics (**e**) of the device, and snapshots of the DFTEM images (**f**–**h**) from Supplementary Video 2 capturing strain-field fluctuations corresponding to the points marked in **e**. **i**, *V*–*t* and *I*–*t* characteristics of the device, and snapshots of DFTEM images and their FFTs (**j**–**l**) from Supplementary Video 3 at the points marked in **i**. The FFTs capture evolution from streaky patterns corresponding to disorder in superstructure reflections (**j**) to a complete loss of intensity in the streaks on SSA (**k** and **l**). Scale bars, 50 nm (**a** and **f**–**h**), 50 nm (**j**–**l**, right).

perpendicular to the nanowire. At the point at which larger fluctuations in current originate (Fig. 4i, point labelled k), corresponding to large strain-field fluctuations in both amplitude and spatial extent (DFTEM image shown in Fig. 4k), these streaky patterns in FFT further lose intensity, becoming more diffuse (Fig. 4k). Eventually, the current reduces (Fig. 4i), with the FFT of the DFTEM image showing only diffuse scattering (Fig. 4l) corresponding to long-range SSA.

Discussion

On the basis of our observations, we propose the following model for amorphization: electric field and carrier wind force provide a driving force for polarization rotation (domain-boundary motion) and sliding fault formation, initially in a local region (nanoscale). The ensuing piezoelectric stress due to polarization rotation creates similar defects over a longer range, dictated by the length scale of mechanical stress. As more sliding faults are created, they interact and cause strain-field fluctuations, which further create (replicate) more sliding faults, leading to much smaller domains (and more domain boundaries). The interaction of many sliding faults and domain boundaries locally causes the loss of long-range order (nanometre-length scale; Fig. 4c), nucleating SSA. These regions are replicated spatially (micrometre-length scales) through long-range strain fields, and this can be construed as multiple nucleation events of the amorphous phase. All these amorphous nuclei locally grow due to acoustic jerks, further disrupting the local crystalline order. Electrically, a collapse of current occurs once the percolative crystalline pathways are cut off completely by the growing amorphous nuclei (Supplementary Note 9). Such long-range electrically induced SSA has not been reported in any other system, which highlights the interplay of unique structure, piezoelectricity and ferroelectricity in β″-In_2Se_3 and the coupling of order parameter to external fields, essential for converting field fluctuations into long-range strain fluctuations.

In conclusion, we uncovered a unique long-range SSA process in ferroelectric β″-In_2Se_3 nanowires on applying a d.c. bias, facilitated by a complex interplay of electric field, current, piezoelectric stress, acoustic jerks and Joule heating. β″-In_2Se_3 is a model material system in which the synergistic confluence of various material properties (layered, semiconducting, ferroelectric and piezoelectric) results in an unconventional amorphization process. We believe that similar studies on other semiconducting ferroic materials can unlock other metastable phase transformations, which holds the potential for designing new materials and devices.

Online content

Any methods, additional references, Nature Portfolio reporting summaries, source data, extended data, supplementary information, acknowledgements, peer review information; details of author contributions and competing interests; and statements of data and code availability are available at https://doi.org/10.1038/s41586-024-08156-8.

1. Wong, H. S. P. et al. Phase change memory. *Proc. IEEE* **98**, 2201–2227 (2010).
2. Nam, S. W. et al. Electrical wind force-driven and dislocation-templated amorphization in phase-change nanowires. *Science* **336**, 1561–1566 (2012).
3. Nukala, P., Lin, C. C., Composto, R. & Agarwal, R. Ultralow-power switching via defect engineering in germanium telluride phase-change memory devices. *Nat. Commun.* **7**, 10482 (2016).
4. Lee, S. H., Jung, Y. & Agarwal, R. Highly scalable non-volatile and ultra-low-power phase-change nanowire memory. *Nat. Nanotechnol.* **2**, 626–630 (2007).
5. Jung, Y., Nam, S. W. & Agarwal, R. High-resolution transmission electron microscopy study of electrically-driven reversible phase change in $Ge_2Sb_2Te_5$ nanowires. *Nano Lett.* **11**, 1364–1368 (2011).
6. Fecht, H. J. Defect-induced melting and solid-state amorphization. *Nature* **356**, 133–135 (1992).
7. Zapperi, S., Cizeau, P., Durin, G. & Stanley, H. E. Dynamics of a ferromagnetic domain wall: avalanches, depinning transition, and the Barkhausen effect. *Phys. Rev. B* **58**, 6353–6366 (1998).
8. Casals, B., Nataf, G. F. & Salje, E. K. H. Avalanche criticality during ferroelectric/ ferroelastic switching. *Nat. Commun.* **12**, 345 (2021).
9. Biroli, G. Disordered solids: in search of the perfect glass. *Nat. Phys.* **10**, 555–556 (2014).
10. Berthier, L. & Biroli, G. Theoretical perspective on the glass transition and amorphous materials. *Rev. Mod. Phys.* **83**, 587–645 (2011).
11. Russo, J., Romano, F. & Tanaka, H. Glass forming ability in systems with competing orderings. *Phys. Rev.* **8**, 021040 (2018).
12. Klement, W., Willens, R. H. & Duwez, P. Non-crystalline structure in solidified gold–silicon alloys. *Nature* **187**, 869–870 (1960).
13. Zhang, L. et al. Amorphous martensite in β-Ti alloys. *Nat. Commun.* **9**, 506 (2018).
14. Rehn, L. E., Okamoto, P. R., Pearson, J., Bhadra, R. & Grimsditch, M. Solid-state amorphization of Zr_3Al: evidence of an elastic instability and first-order phase transformation. *Phys. Rev. Lett.* **59**, 2987–2990 (1987).
15. Bridges, F. et al. Local vibrations and negative thermal expansion in ZrW_2O_8. *Science* **280**, 886–890 (1998).
16. He, Y. et al. In situ observation of shear-driven amorphization in silicon crystals. *Nat. Nanotechnol.* **11**, 866–871 (2016).
17. Shportko, K. et al. Resonant bonding in crystalline phase-change materials. *Nat. Mater.* **7**, 653–658 (2008).
18. Nukala, P. et al. Inverting polar domains via electrical pulsing in metallic germanium telluride. *Nat. Commun.* **8**, 15033 (2017).
19. Edwards, A. H. et al. Electronic structure of intrinsic defects in crystalline germanium telluride. *Phys. Rev. B* **73**, 045210 (2006).
20. Lines, M. E. & Glass, A. M. *Principles and Applications of Ferroelectrics and Related Materials* (Oxford Univ. Press, 2001).
21. Ding, W. et al. Prediction of intrinsic two-dimensional ferroelectrics in In_2Se_3 and other III_2-VI_3 van der Waals materials. *Nat. Commun.* **8**, 14956 (2017).
22. Xiao, J. et al. Intrinsic two-dimensional ferroelectricity with dipole locking. *Phys. Rev. Lett.* **120**, 227601 (2018).
23. Xu, C. et al. Two-dimensional antiferroelectricity in nanostripe-ordered In_2Se_3. *Phys. Rev. Lett.* **125**, 47601 (2020).
24. Xu, C. et al. Two-dimensional ferroelasticity in van der Waals β′-In_2Se_3. *Nat. Commun.* **12**, 3665 (2021).
25. Zhang, Z. et al. Atomic visualization and switching of ferroelectric order in β-In_2Se_3 films at the single layer limit. *Adv. Mater.* **34**, 2106951 (2022).
26. Wang, L. et al. In-plane ferrielectric order in van der Waals β′-In_2Se_3. *ACS Nano* **18**, 809–818 (2024).
27. Peng, H., Schoen, D. T., Meister, S., Zhang, X. F. & Cui, Y. Synthesis and phase transformation of In_2Se_3 and $CuInSe_2$ nanowires. *J. Am. Chem. Soc.* **129**, 34–35 (2007).
28. Liu, L. et al. Atomically resolving polymorphs and crystal structures of In_2Se_3. *Chem. Mater.* **31**, 10143–10149 (2019).
29. Van Landuyt, J., Hatwell, H. & Amelinckx, S. The domain structure of β-In_2S_3 'single crystals' due to the ordering of indium vacancies. *Mater. Res. Bull.* **3**, 519–528 (1968).
30. Van Landuyt, J. & Amelinckx, S. Antiphase boundaries and twins associated with ordering of indium vacancies in β-In_2S_3. *Phys. Status Solidi B Basic Solid State Phys.* **31**, 589–600 (1969).
31. Chen, P. J. & Montgomery, S. T. A macroscopic theory for the existence of the hysteresis and butterfly loops in ferroelectricity. *Ferroelectrics* **23**, 199–207 (1980).
32. Modi, G., Stach, E. A. & Agarwal, R. Low-power switching through disorder and carrier localization in bismuth-doped germanium telluride phase change memory nanowires. *ACS Nano* **14**, 2162–2171 (2020).
33. Modi, G. et al. Controlled self-assembly of nanoscale superstructures in phase-change Ge–Sb–Te nanowires. *Nano Lett.* **24**, 5799–5807 (2024).
34. Yan, Z. H., Klassen, T., Michaelsen, C., Oehring, M. & Bormann, R. Inverse melting in the Ti-Cr system. *Phys. Rev. B* **47**, 8520–8527 (1993).
35. Li, W., Qian, X. & Li, J. Phase transitions in 2D materials. *Nat. Rev. Mater.* **6**, 829–846 (2021).
36. Matzen, S. et al. Super switching and control of in-plane ferroelectric nanodomains in strained thin films. *Nat. Commun.* **5**, 4415 (2014).
37. Gao, P. et al. Revealing the role of defects in ferroelectric switching with atomic resolution. *Nat. Commun.* **2**, 591 (2011).
38. Fu, H. & Cohen, R. E. Polarization rotation mechanism for ultrahigh electromechanical response. *Nature* **403**, 281–283 (2000).
39. Salje, E. K. H., Wang, X., Ding, X. & Scott, J. F. Ultrafast switching in avalanche-driven ferroelectrics by supersonic kink movements. *Adv. Funct. Mater.* **27**, 1700367 (2017).
40. Sui, F. et al. Atomic-level polarization reversal in sliding ferroelectric semiconductors. *Nat. Commun.* **15**, 3799 (2024).

Methods

Synthesis of In_2Se_3 nanowires

In_2Se_3 nanowires in the β″-phase (Supplementary Fig. 1) were grown by a catalyst-assisted vapour–liquid–solid mechanism. An approximately 5-nm-thick Au–Pd catalyst layer was sputtered on a silicon substrate and was used for nanowire growth. The Au–Pd film breaks down into catalyst nanoparticles on heating in the furnace. About 10 mg of In_2Se_3 powder (Sigma-Aldrich) was placed at the centre of a 2.54-cm tube furnace (Lindberg/Blue M), whereas the silicon substrate was placed approximately 10 cm downstream from the centre of the furnace. Before starting nanowire growth, the furnace was flushed multiple times with argon gas until a pressure of approximately 30 mtorr was reached to remove any residual oxygen. After that, the argon flow rate was set to 120 s.c.c.m. and the tube pressure was stabilized at approximately 50 torr. The furnace temperature was set to 700 °C and nanowire growth was carried out for 5 h, after which the furnace was gradually cooled down to room temperature.

Device fabrication

Electrical devices were fabricated on circular TEM grids (diameter, 3.05 mm) from Ted Pella with a 0.25 mm × 0.25 mm silicon nitride (SiN_x) membrane in the centre (Supplementary Fig. 11). Electron-beam lithography was used to pattern the electrodes on the TEM grids. First, the TEM grid was spin coated with two layers (approximately 50 nm each) of PMMA 950 A2 resist with resist baking at 180 °C after each spin coat. A pre-defined array of electrodes was patterned by electron-beam lithography, followed by the physical vapour deposition of approximately 10 nm Ti and around 30 nm Au. A TESCAN S8000X focused ion beam (FIB) was used to pattern trenches (width, approximately 1–2 μm; length, around 60 μm) in between the metal electrodes to enable HRTEM imaging. Following that, nanowires were dry transferred by gently tapping the patterned TEM grids on the nanowire growth substrate. Final electrical connections were established by depositing platinum through FIB at the point of contact of the nanowire with the patterned electron-beam lithography electrodes. The time and area of FIB exposure were carefully controlled to avoid any material damage from the ion beam. The open and lateral device geometry of the nanowires and their single-crystalline structure offer a favourable material system to image the evolution of the microstructure with high spatial resolution, as well as simultaneously minimizing the effects of pre-existing grain and domain boundaries on the structural dynamics.

Electrical characterization of devices

All the electrical measurements were performed in a two-probe configuration on a Lake Shore TTPX cryogenic probe station. The d.c. *I*–*V* sweeps were applied using a Keithley 2602 source meter. For monitoring the evolution of current with time as the d.c. voltage is held constant, we used an electrical setup shown in Supplementary Fig. 21. A constant d.c. bias was applied to the nanowire device connected in series with a standard 1 MΩ resistor through a Keithley 2635B source measure unit. Current was indirectly measured as the voltage drop across the standard resistor using a 500 MHz Tektronix DPO3052 digital oscilloscope with a 1 MΩ impedance. Hence, the actual current through the nanowire (Extended Data Fig. 1) is twice that indicated in Extended Data Fig. 1, but for the sake of proportionality, the actual magnitude of current is not as important.

HAADF-STEM imaging and Se displacement mapping

The imaging was carried out on an aberration-corrected Titan Themis instrument, which was operated at 300 kV. A probe angle of 24 mrad was used for imaging the nanowires in the STEM mode with a HAADF collection angle of 48–200 mrad. The obtained HR images were further processed to get enhanced contrast of dislocations by first Bragg filtering the raw image (Supplementary Fig. 19a–c) and overlaying this image with the inverse FFT image (Supplementary Fig. 19d,e) obtained by masking only the spots given by band periodicity to obtain the final dislocation-contrast-enhanced images (Supplementary Fig. 19f). For mapping the Se displacement vector, we first found the geometric centre of each hexagon and then subtracted it from the central Se positions by using atom finding and refining algorithms from Atomap[41]. In this way, Se displacements from their geometric centres were mapped.

PFM switching

In_2Se_3 nanowires were transferred to Si substrates sputtered with gold and clamped at the ends by depositing platinum in an FIB Helios 5 UX DualBeam instrument. PFM spectroscopy measurements were carried out on AFM Asylum Research MFP-3D Origin+ in the dual-amplitude resonance tracking mode. The nanowires were mapped using the tapping mode followed by Dual AC Resonance Tracking PFM spectroscopy measurements by moving the tip to the points of interest. Voltage pulses were applied with amplitude varying from 0 to V_{max}, V_{max} to $-V_{max}$ and $-V_{max}$ to 0 (sawtooth envelope). The amplitude and phase of the piezoresponse is measured when every pulse is on (field-on response) and after a short delay, once the pulse is turned off (field-off response). The remnant loops (field off) of amplitude (Supplementary Fig. 9a) and phase (Supplementary Fig. 9b) show that the displacements are consistent with the polarization-switching behaviour.

In situ TEM measurements

The in situ TEM heating experiment (Supplementary Video 4) was performed on a JEOL F200 STEM instrument in the TEM/diffraction mode. The nanowires were dry transferred on a Hummingbird Scientific heating chip (Supplementary Fig. 23a) by gently tapping the TEM chip on the nanowire growth substrate. A specialized single-tilt heating/biasing TEM holder from Hummingbird Scientific was used to monitor the structural changes during the in situ heating experiment. Temperature calibration was received from the manufacturer to achieve controlled heating based on the resistance measurements, for which the current was applied through an externally connected power supply.

In situ TEM electrical biasing experiments (Supplementary Videos 1–3) were performed on a Thermo Fisher Titan Themis 300 instrument, in the DFTEM and diffraction modes. Nanowires were transferred onto the microelectromechanical-systems-based biasing chip (DENSsolutions), and contacts were made to the metal pads on the chip through FIB. The chip was then loaded onto a lightning biasing holder (DENSsolutions), which was externally connected to a Keithley parameter analyser (Model 4200) for electrical measurements. The DFTEM images/videos were simultaneously captured as the devices were electrically biased in two modes: (1) constant voltage as a function of time and (2) linear ramp of voltage as a function of time. Sampling time for both electrical data and DFTEM images was set to be the same. The application of bias results in small mechanical motion of the nanowire, which is used to synchronize the electrical stimulus with the DFTEM images.

DFT calculations

The thermodynamic stability and phase transformation between In_2Se_3 polymorphs were calculated using spin-polarized DFT and the preferred potential[42,43] machine learning potential implemented in the Matlantis program, respectively. The DFT calculations were performed with the projector augmented wave[44] method and the Perdew–Burke–Ernzerhof[45] exchange–correlation functional of the generalized gradient approximation using the Vienna ab initio simulation package[46,47]. Monkhorst–Pack grids of 10 × 6 × 10 *k*-points, energy convergence criteria of 10^{-5} eV and force convergence criteria of 0.02 eV $Å^{-1}$ were applied. Our DFT calculations assume a temperature of 0 K, but vibrational free-energy contribution at room temperature and higher temperatures can stabilize the initial structure. Moreover, it is possible to observe thermodynamically metastable configurations in experiments, depending on the external mechanical, thermal and electrical driving

conditions, which can drive the system out of equilibrium. The activation barriers for phase transformation between In_2Se_3 polymorphs were obtained using the climbing image nudged elastic band[48] method with a convergence criterion of 0.1 eV $Å^{-1}$. The DFT-trained machine learning potential is a universal interatomic potential[43], and is accurate enough to describe the saddle energy barriers. It should be noted that for the sake of computational simplicity, we did not consider the In and Se vacancies in our structures for DFT calculations (Supplementary Note 10).

Data availability

The datasets generated and analysed during the current study are included with the Article or available from the corresponding authors upon reasonable request. Source data are provided with this paper.

41. Nord, M., Vullum, P. E., MacLaren, I., Tybell, T. & Holmestad, R. Atomap: a new software tool for the automated analysis of atomic resolution images using two-dimensional Gaussian fitting. *Adv. Struct. Chem. Imaging* **3**, 9 (2017).
42. Takamoto, S. et al. Towards universal neural network potential for material discovery applicable to arbitrary combination of 45 elements. *Nat. Commun.* **131**, 2991 (2022).
43. Takamoto, S., Okanohara, D., Li, Q. J. & Li, J. Towards universal neural network interatomic potential. *J. Mater.* **9**, 447–454 (2023).
44. Kresse, G. & Joubert, D. From ultrasoft pseudopotentials to the projector augmented-wave method. *Phys. Rev. B* **59**, 1758 (1999).
45. Perdew, J. P., Burke, K. & Ernzerhof, M. Generalized gradient approximation made simple. *Phys. Rev. Lett.* **77**, 3865 (1996).
46. Kresse, G. & Hafner, J. Ab initio molecular dynamics for liquid metals. *Phys. Rev. B* **47**, 558 (1993).
47. Kresse, G. & Furthmüller, J. Efficient iterative schemes for ab initio total-energy calculations using a plane-wave basis set. *Phys. Rev. B* **54**, 11169 (1996).
48. Henkelman, G., Uberuaga, B. P. & Jónsson, H. A climbing image nudged elastic band method for finding saddle points and minimum energy paths. *J. Chem. Phys.* **113**, 9901–9904 (2000).

Acknowledgements This work was supported by the ONR-MURI (grant no. N00014-17-1-2661) and partially supported by the US NSF (FuSe; no. 2328743), US Air Force Office of Scientific Research (award no. FA9550-23-1-0189) and ANRF-SERB:CRG/2022/003506, Government of India. Support from NSF-MRSEC/DMR-2309043 seed grant is also acknowledged. P.N. acknowledges Indian Institute of Science (IISc) start-up seed grant and Infosys young researcher award. Electron microscopy and PFM measurements were carried out at the Advanced Facility for Microscopy and Microanalysis and the Micro Nano Characterization Facility in IISc. Device fabrication work and electron microscopy was conducted at the Singh Center for Nanotechnology, which is supported by the NSF National Nanotechnology Coordinated Infrastructure Program under grant no. NNCI-2025608 and through the University of Pennsylvania Materials Research Science and Engineering Center (MRSEC) (grant no. DMR-1720530). P.N. and S.K.P. are grateful for the support received from V. Dey in setting up a robust biasing system for the in situ TEM experiments.

Author contributions G.M. and R.A. conceptualized the project, and along with P.N. and S.K.P., designed the experiments and analysed the data. G.M. performed the nanowire synthesis, device fabrication, electrical characterization, in situ and ex situ TEM experiments, device modelling and finite element analysis. S.K.P. and P.N. performed the ex situ HAADF-STEM imaging, and in situ DFTEM biasing experiments. C.K. and J.L. carried out the DFT calculations. A.C.M. helped with the four-dimensional STEM polarization mapping. U.K. helped with the nanowire synthesis. A.T. and P.N. performed the PFM measurements and analysis. J.H. assisted with the in situ TEM heating setup. E.A.S. provided suggestions for the TEM characterization. P.K.D. helped with the structure interpretation and data analysis. G.M. and R.A. wrote the manuscript with inputs from S.K.P. and P.N. All authors discussed the results and commented on the final manuscript.

Competing interests E.A.S. is an equity holder in Hummingbird Scientific. The other authors declare no competing interests.

Additional information

Supplementary information The online version contains supplementary material available at https://doi.org/10.1038/s41586-024-08156-8.

Correspondence and requests for materials should be addressed to Pavan Nukala or Ritesh Agarwal.

Peer review information *Nature* thanks Junwei Zhang and the other, anonymous, reviewer(s) for their contribution to the peer review of this work. Peer reviewer reports are available.

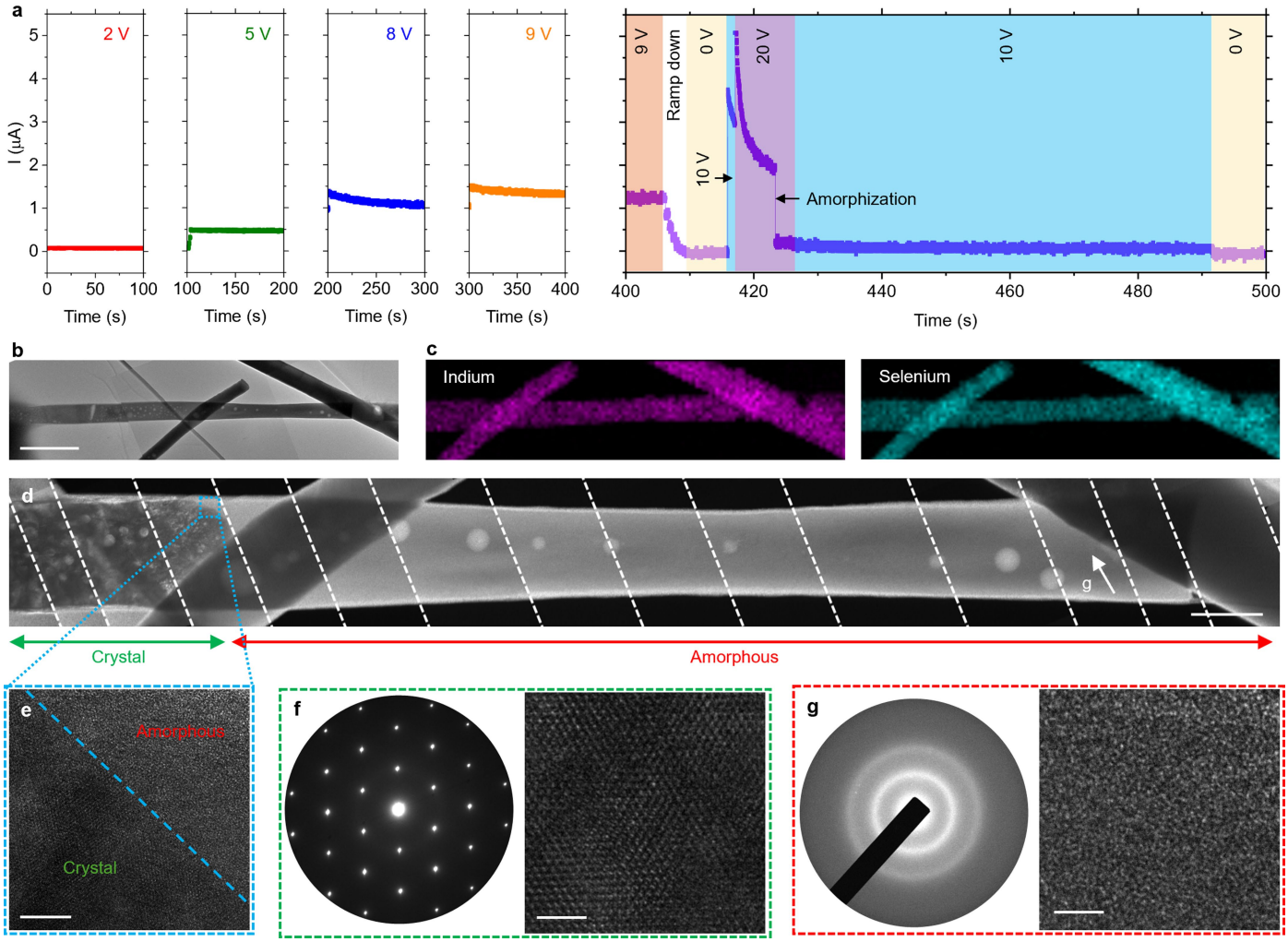

Extended Data Fig. 1 | TEM characterization of amorphized β″-In_2Se_3 nanowire device upon application of d.c. voltage. (**a**) Evolution of current in the nanowire device with time when the device is held at different fixed d.c. voltages. Amorphization occurs at 20 V and is preceded by a rapid decrease in current with time. (**b**) Low magnification TEM image of the nanowire device after amorphization. (**c**) EDX elemental mapping of indium and selenium in the amorphized region of the nanowire. (**d**) DF-TEM image of the nanowire after amorphization. The contrast from the crystal-amorphous interface can be seen at the left side of the nanowire, where a part of the interface is shown in the HR-TEM image in (**e**). Electron diffraction and HR-TEM image from the (**f**) paraelectric crystalline phase and (**g**) amorphous regions of the nanowire device. The dashed white lines in (d) indicate the regions where the images were combined. Scale bars: (b) 1 μm, (d) 200 nm, (e) 5 nm, (f) and (g) 2 nm.

nature portfolio

https://doi.org/10.1038/s41586-024-08156-8

Supplementary information

Electrically driven long-range solid-state amorphization in ferroic In_2Se_3

In the format provided by the authors and unedited

Supplementary Materials for

Electrically-driven long range solid state amorphization in ferroic In_2Se_3

Gaurav Modi,[1#] Shubham K. Parate,[2#] Choah Kwon,[3] Andrew C. Meng,[1] Utkarsh Khandelwal,[1] Anudeep Tullibilli,[2] James Horwath,[1] Peter K. Davies,[1] Eric A. Stach,[1] Ju Li,[3] Pavan Nukala[2*] and Ritesh Agarwal[1*]

[1]Department of Materials Science and Engineering, University of Pennsylvania, Philadelphia, Pennsylvania 19104, USA

[2]Centre for Nanoscience and Engineering, Indian Institute of Science, Bengaluru, Karnataka 560012, India

[3]Department of Materials Science and Engineering, Massachusetts Institute of Technology, Cambridge, Massachusetts 02139, USA

[#] These authors contributed equally to this work

*Corresponding authors: riteshag@seas.upenn.edu, pnukala@iisc.ac.in

This file includes:

Supplementary text

Figures S1-S30

Caption for Movies S1-S4

Other supplementary materials for this manuscript include the following:

Movie S1-S4

Supplementary Text:

Supplementary Note 1: Crystal structure of 2D β′-In_2Se_3 and β″-In_2Se_3:

To understand how the nanomaterial geometry can influence the configuration of the electric dipoles, we need to consider the fact that the ferroelectricity in In_2Se_3 also has an associated ferroelasticity.[1] Hence, it is likely that the nanowire geometry and the associated strain relaxation from the surfaces is one of the factors responsible for the ferroelectric arrangement of electric dipoles in the nanowires, where the polarization points along the $< 1\ \bar{1}\ 0\ 0 >$ direction, perpendicular to the crystal facets. However, it should be emphasized that depending on the relative magnitude of polarization induced by In/Se vacancy ordering vs. the Se displacement induced polarization, β″-In_2Se_3 could either be ferroelectric or ferrielectric. However, in our schematic in **fig. 1f**, we assumed that the magnitude of the vacancy ordering induced polarization is smaller than the Se displacement induced polarization, hence, it is more appropriate to classify β″-In_2Se_3 as a ferroelectric material.

Synthesis of nanowires was performed at a local substrate temperature of ~400-450 ºC ($T>T_{Curie}$ ~220 ºC), hence, at the time of synthesis a paraelectric crystal was nucleated. However, cooling of the sample post-synthesis resulted in the nucleation of a single-domain β″-In_2Se_3 ferroelectric phase starting from the surface due to the lower energy barrier for nucleation and stress relaxation from the surfaces. However, this is not the case in 2D flakes of β′-In_2Se_3, therefore there it results in the formation of an antiferroelectric/ ferrielectric order with three possible domains, where polarization in each nanostripe points along a $< 1\ \bar{1}\ 0\ 0 >$ direction. Thus, overall, the ferroic order is different in nanowires and flakes and has a direct correlation to the number of superlattice reflections in the SAED. However, it is also possible that in 2D flakes of β′-In_2Se_3, both kinds of superlattice periodicities and ferroic order coexist as has been shown in other studies.[2,3]

Convergent beam electron diffraction (CBED) is a good indicator of the 'local' crystal symmetry[4] and hence we used CBED as a probe to further illustrate the different electrical polarization arrangements in 2D β′-In_2Se_3 and β″-In_2Se_3. Xu et al.[5] observed the presence of a vertical $\{1\ 0\ \bar{1}\ 0\}$ mirror plane in the CBED intensity but we propose that the dipole arrangement in β″-In_2Se_3 is ferroelectric as shown in the schematic in **fig. 1f** of the main text, hence resulting in a horizontal $\{1\ 1\ \bar{2}\ 0\}$ mirror plane (**fig. S6** and **fig. 1d**). However, the ferroelectric polarization order in the nanowires might be a metastable state. After annealing of the as-synthesized nanowires at 190 ºC ($T<T_{Curie}$) for 6 hours under vacuum and inert gas argon flow, we observed that the structure evolves after annealing and now we also see the presence of n>3 superlattice reflections in the SAED between the fundamental rhombohedral reflections (**fig. S20a**). Additionally, we also observe that the superlattice reflections now are present along all the three $< 1\ \bar{1}\ 0\ 0 >$ directions instead of just along the growth direction of the nanowires because of formation of multiple domains. Due to the presence of a mixture of superlattice periodicities and dipole arrangements

after annealing, the CBED pattern also indicates the lack of any identifiable symmetry operations (**fig. S20b**).

Supplementary Note 2: DFT calculations for crystal structure stability of β″-In_2Se_3:

We performed density functional theory (DFT) calculations to validate the stability of the new crystal structure of β″-In_2Se_3 nanowires. Calculations show that the formation energy (starting from paraelectric β-phase) with $< 1\bar{1}00 >$ direction of Se displacement (-68.74 meV/f.u.) is comparable with $< 11\bar{2}0 >$ direction of Se displacement (-71.04 meV/f.u.) for 1T stacking configuration (**fig. S10a**). Activation energy barrier calculations using DFT trained machine learning potentials show a barrierless transformation from 1T β-β" In_2Se_3 (**fig. S10b**), supporting the presence of spontaneous polarization along $< 1\bar{1}00 >$. Similar formation energy for 1T (-68.74 meV/f.u.) and 2H stacking configurations (-69.47 meV/f.u.) of β″-In_2Se_3 from their respective paraelectric β-phase, further supports the stability of 1T stacking (**fig. 1h**).

Supplementary Note 3: Constant d.c. voltage ex-situ TEM and no bias in-situ TEM heating experiments: Evidence that Joule heat is not the primary driving force for amorphization:

Since the nanowires amorphized after exhibiting NDR accompanied by creation of sliding faults and nanoscopic domains, we examined another device to correlate the evolution of defects, device resistance and eventual amorphization. For this experiment, the d.c. voltage was held at a fixed value for few tens of seconds and increased in steps, while monitoring the current (**Ext. fig. 1a**; **fig. S21**). We first applied a series of I-V sweeps until we observed NDR and prepared the device in a state with defects (**fig. S22**). In this state, on holding the d.c. voltages at lower values (≤5V), the current did not change over time; however, at intermediate voltages (8-9V) the current decreased slowly (≤3.2 nA/s) (**Ext. fig. 1a**). However, at higher bias (10-20V), a rapid non-linear decrease in current was observed because of defect-induced carrier mobility reduction (SI **note 5**). Following a rapid decrease of current at 20V, a sudden current drop was observed, indicating amorphization. Bright and DF-TEM imaging (**Ext. fig. 1b-d**) shows that most of the nanowire suspended over the trench had amorphized. HR-TEM image of clean crystal-amorphous interface (**Ext. fig. 1e**) and SAED from the remaining crystalline region (**Ext. fig. 1f**) showed that the superlattice reflections disappeared and a paraelectric β-phase had formed. The superstructure contrast modulation observed in pristine nanowires also disappeared from the HRTEM image (**Ext. fig. 1f**). SAED and HR-TEM images from the amorphous region of the nanowire (**Ext. fig. 1g**) show the characteristic diffuse halo and lack of crystalline fringes, respectively.

Considering that the thermal time constant of the In_2Se_3 nanowires is <0.2 ms (see SI **note 4**), it can be safely assumed that the Joule heating rate in the nanowires is very fast compared to the rate of sliding faults generation. However, amorphization occurred after a time delay of ~6.2 s after applying a bias of 20V (**Ext. fig. 1a)**. This observation reaffirms that heating (temperature)

alone is not the sole driving force for amorphization, and a critical density of defects must be accumulated before amorphization. The accumulation of defects results in an order-disorder transition, which can either be a β″-β transition (for lower defect density, polarization order-disorder) or alternatively a crystal-amorphous transition (for higher defect density, structural order-disorder). However, the kinetics of defect generation is further dependent on the temperature in each region of the nanowire upon applying a d.c. voltage (**fig. S13**), hence amorphization usually occurs in the middle region of the nanowire where the temperature is highest.

Depending on the electrical biasing history of the nanowire devices, the polarization order in the untransformed crystalline region, adjacent to the amorphized region, was observed to vary. Although at first glance, the appearance of a paraelectric β-phase in the remaining crystalline region in **Ext. fig. 1f** may seem to be in contradiction with the residual superstructure ordering in **fig. 2l** of main text, it can be explained well if we compare the electrical history of these two nanowire devices. For the nanowire device in **fig. 2**, the d.c. voltage was applied in continuous sweeps, where each sweep lasted for only a few seconds (<2s). On the other hand, the device in **Ext. fig. 1** was subjected to higher magnitude d.c. voltages for a much longer duration. Hence, the device in **Ext. fig. 1** accumulates an overall higher density of dislocations which are relatively more evenly distributed throughout the length of the nanowire suspended on the trench. Hence, the remnant crystalline region in the nanowire device in **Ext. fig. 1** underwent a polarization disordering as the adjacent region underwent a structural disordering to form an amorphous phase. It should also be noted that the voltage/current at which amorphization occurs is sensitive to the electrical history of the material because the generation of defects is dependent on both the magnitude of the voltage and the time for which it is applied. Hence depending on how the d.c. voltage is applied (single or multiple I-V sweeps or sudden step-like increase), the amorphization current and voltage can be different (as also seen in **figs. 2-4** and **Ext. fig. 1**).

To further decouple the effects of the electrical and thermal stimuli, we performed in-situ TEM heating experiments, where we only observed β″-β phase transition (~250ºC) instead of amorphization (**fig. S23**; **movie S4**), suggesting that the electrically induced defects are necessary for amorphization. Furthermore, heating of the nanowires at 190ºC in a furnace under an inert environment (under Ar gas flow) resulted in growth of other ferroic domains without any amorphization (**fig. S20**). Therefore, a multimodal coupling between ferroelectric ordering with electric field/ current, piezoelectric stress and current-induced Joule heating is responsible for the amorphization of β″-In_2Se_3 nanowires.

Supplementary Note 4: Estimating the thermal time constant for the In_2Se_3 nanowire in fig. 2 of main text:

Thermal conductivity: κ = 0.25-3.5 $W.m^{-1}K^{-1}$ (ref. 17)

Nanowire length between electrodes: l = 5.6 μm

Nanowire cross-section area: A = 160 nm X 160 nm

Material density: ρ = 5800 kg.m^{-3}

Thermal capacity: C_p = 268 J.Kg^{-1}K^{-1} (ref. 16)

Thermal resistance: $R_{th} = {}^{l}/_{\kappa . A} = 6.25\ X\ 10^{7} - \ 8.75\ X\ 10^{8}\ K.s.J^{-1}$

Thermal capacitance: $C_{th} = \rho . V . C_p = 2.23\ X\ 10^{-13}\ J.K^{-1}$

Thermal time constant: $R_{th}.C_{th}$ = **13.9 - 195 µs**

Supplementary Note 5: Theoretical modeling of observed I-V behavior in β″-In_2Se_3 nanowires:

(i) For d.c. I-V sweep measurements: Assuming defect concentration D varies exponentially with electric field $E(t)$ and $0 - t_1$ is the time in which $E(t)$ was swept from $0 - E_0$ via the following equations, where D_0 and A_0 are constants, and E_T is the threshold electric field:

$$E(t) = E_0 \frac{t}{t_1}$$

$$D = \int D_0 e^{A_0\left(\frac{E(t)}{E_T} - 1\right)} . dt$$

$$D = \frac{E_T t_1}{A_0 E_0} D_0 e^{A_0\left(\frac{E_0\ t}{E_T t_1} - 1\right)} + I$$

Assuming carrier mobility μ varies linearly with defect concentration D via the following equation (**fig. S15a**), where m and μ_0 are constants:

$$\mu = \mu_0 - mD$$

Assuming current density j varies with the electric field E via the following equation (**fig. S24**), where σ is the electrical conductivity, n is the carrier density and e is the elementary charge.

$$j = \sigma E = ne\mu E$$

Values used in calculations (all in SI units): $D_0 = 1$, $A_0 = 7$, $E_0 = 1$ $E_T = 0.5$, $\mu_0 = 200$, $m = 1$, $ne = 1$, $t_1 = 1$ and integration constant $I = 0$

(ii) For measurements where d.c. voltage was increased in steps but was held constant for a given step time duration:

$$E(t) = E_i\ (constant)$$

The defect concentration equation can be modified as follows:

$$D = \sum_{i=1}^{n} \int_{t_{i-1}}^{t_i} D_0 e^{A_0(\frac{E_i}{E_T}-1)} . dt$$

Electric field E (in SI units) is as follows:

$$E_1 = 0.2, \qquad 0 < t < 2.5s$$
$$E_2 = 0.4, \qquad 2.5s < t < 5.0s$$
$$E_3 = 0.6, \qquad 5.0s < t < 7.5s$$
$$E_4 = 0.8, \qquad 7.5s < t < 10.0s$$

For the above stepwise electric field, the defect density can be expressed as (**fig. S25**):

$$D = \sum_{i=1}^{n} D_0 e^{A_0\left(\frac{E_i}{E_T}-1\right)}(t_i - t_{i-1})$$

Values used in calculations (all in SI units): $D_0 = 1$, $A_0 = 5$, $E_0 = 1$ $E_T = 0.5$, $\mu_0 = 200$, $m = 1$ and $ne = 1$

Supplementary Note 6: Formation mechanism of various nanoscopic domains in d.c. biased β″-In_2Se_3 nanowires

The nanoscopic domains in d.c. biased β″-In_2Se_3 nanowires are formed by interlayer sliding of the quintuple In_2Se_3 layers with respect to each other by different lattice and sub-lattice vectors (**fig. 3h-i and S27-S28**). For example, in **fig. 3f**, region D5 can be simulated as an overlay of at least two different crystals (**fig. 3i**) displaced from each other by a net slip vector of $\vec{a}/n_1 + \vec{b}/n_2$ (n_1 and n_2 are integers). Such a net slip vector can be generated by interaction of several stacking faults, with slip vectors parallel to the vdW layers.

Fig. S27 (b-c) shows that the sliding defect can be generated from a slip of a part of the crystal along the vdW layer by $2\vec{b}$ (as per the vector notation described in **fig. S26**). This is an APB that generates a lattice slip with a phase difference of π (with lattice periodicity vector being $4\vec{b}$), with respect to the matrix (unslipped lattice). A closer inspection of such APBs reveals the existence of two partial dislocations on either side of the APB (with Burgers vectors $\vec{B} = 2\,\vec{b}$), as depicted schematically in **fig. S27c** (when viewed along c-axis). Hence, these sliding faults in the initial stages can alternatively be interpreted as superlattice dislocations (**fig. S27**). However, in later stages many of such sliding faults start interacting, with each other giving rise to nanoscopic sliding domains, which are also coupled to polarization domains.

Another nanoscopic region we identified (D2 in **fig. 3f**) can be explained by a stacking configuration where every alternate quintuple layer in the parent 1T β″-In_2Se_3 is displaced by $2/3\,\vec{b}$

(**fig. 3h**). The projection of the crystal along the $\vec{c}$-axis (**fig. S28d**) shows the mechanism of contrast inversion observed in the HRSTEM image for this D2 region as compared to the pristine nanowire. Our calculations show that the activation barrier for the 1T to D2 stacking transformation by interlayer sliding is only 149.1 meV (**fig. 3g**), which can help to nucleate this D2 configuration easily under the influence of d.c. bias.

The same region D2, alternatively, can also represent the conversion of 1T phase with a stacking sequence ABCAB ABCAB to 2H phase with stacking sequence ABCAB CBACB (**fig. S28c**). Such a transformation is akin to formation of twins in metals that nucleate with successive partials (in this case combination of intralayer slip vectors $\frac{4}{3}\vec{b}$, 0, $-\frac{4}{3}\vec{b}$, $\frac{4}{3}\vec{b}$ and 0 in Se, In, Se, In and Se quintuple layer gives rise to this transformation). Although our DFT calculations suggest that the activation barrier for 1T to 2H transition is 1.68 eV (**fig. S10c**), we believe that the large strain in the system present because of interaction of several sliding domains can let the system overcome this barrier, nucleating the 2H phase. Such a transformation will be facilitated by the elastic strain generated from many interlayer sliding faults. We believe that the In and Se vacancy-rich layers can further lower the energy barrier for local atomic rearrangement for the creation of nanoscopic domains of various polarization and stacking configurations and polymorphs of In_2Se_3.

Supplementary Note 7: Impact on interlayer sliding by electric current direction relative to the crystal axes:

By increasing the growth temperature, we synthesized nanowires grown along the $\vec{c}$-axis, but notably for these nanowires with carrier-wind perpendicular to the vdW planes, no structural changes occurred during biasing (**fig. S29**). SSA occurs only when the field/current is applied parallel to the vdW layers, underscoring the role of interlayer sliding and polarization rotation for amorphization. Hence, a synergistic confluence of various material properties in β″-In_2Se_3 such as: (i) an optimal electrical conductivity induced carrier-lattice coupling for vdW interlayer sliding, (ii) Electric field-ferroelectric order coupling induced lowering of interlayer sliding activation barrier, polarization rotation and piezoelectric stress, and (iii) In/Se vacancy-rich layers mediated faster diffusion kinetics for local atomic rearrangement facilitates the SSA process. This is perhaps why SSA has not yet been reported in other layered systems (SI **note 8; fig. S30**).

Supplementary Note 8: Comparison of electrically induced vdW interlayer sliding in β″-In_2Se_3 nanowires with other vdW ferroelectric materials and its role in amorphization:

In recent years, interlayer sliding has been observed as a mechanism for out-of-plane polarization reversal in some vdW ferroelectric materials.[6] However, multiple polarization configurations and rotation which results in large piezoelectric stress, ensuing polarization

frustration and domains (coupled to the sliding faults) and long range amplification of all these features by stress and acoustic jerks is unique to this system.

The differences in the interlayer sliding between β″-In_2Se_3 and other such vdW ferroelectrics is illustrated in the following:

i. Firstly, the spontaneous polarization direction in β″-In_2Se_3 is in the *a-b* plane, and based on our DFT calculations, it can have twelve nearly-degenerate polarization states along $< 1\,1\,\bar{2}\,0 >$ or $< 1\,\bar{1}\,0\,0 >$ depending on the direction of in-plane Se displacement (**fig. 3g** and **fig. S10a**).[5] On the other hand, majority of other vdW sliding ferroelectrics have a net polarization simply by virtue of their stacking sequence (even if each individual layer is centrosymmetric) and the associated interfacial charge transfer. Therefore, the polarization direction is along the c-axis and can only have two possible polarization states.[6] In such sliding ferroelectrics, when an electric field is applied vertically along the c-axis, it causes horizontal interlayer sliding along the a-b plane as shown in **fig. S30**. Therefore, the driving force for such horizontal interlayer sliding is polarization reversal induced by the 'vertical' electric field. Since both the possible polarization states have well-defined atomic stacking corresponding to each polarization direction, it results in a coordinated interlayer sliding, where the inter-layer registry between the different layers is still maintained. On the other hand, in β″-In_2Se_3 we observe vdW interlayer sliding when a 'horizonal' electric field is applied along the a-axis direction where the driving force is the carrier-wind force but the coupling of the electric field with polarization also reduces the barrier for interlayer sliding (**fig. 3g** and **fig. S10d**). *Because of the plethora of possible polarization states, the material locally 'slips' along various directions on the a-b plane, creating several sliding faults, frustrated domains and domain boundaries*. Such seemingly random slipping causes loss of interlayer registry as we also see in the HAADF-STEM images of the d.c.-biased nanowires (**fig. 3f**). The intersection region of several such sliding faults causes local loss of long-range crystalline order, which is replicated in much larger scale by the piezoelectric stress and acoustic jerks caused by interaction between domain boundaries.

ii. It is well known in ferroelectrics that large number of polarization configurations causes large piezoelectric stress and resulting jerks from dynamics of domains. Although interlayer sliding in context of ferroelectric switching between two polarizations states is observed in other sliding ferroelectrics, we emphasize that plethora of polarization configurations is unique to this system among the set of all the 2D sliding ferroelectrics discovered, and so is the stress induced amplification of the faults and resulting loss of crystallinity.

Supplementary Note 9: Some extra notes on in-situ TEM observations of SSA:

Understanding the initial state of the nanowire: We present new data on in situ biasing on a non-pristine nanowire, with some prior electrical history. The following features on this nanowire need to be understood to glean insights from the in-situ biasing videos **(Movie S1-S3)**.

1. Initial diffraction and DFTEM images reveal that the superstructure ordering (due to In and Se vacancy bands) perpendicular to the growth axis of pristine wire is intact. However, it is perturbed by sliding faults apparent from the DFTEM images (feature 1, **fig. S17b**) as well as additional superstructure reflections about major Bragg peaks (feature 2, **fig. S17c**). These patterns correspond to localized regions with vacancy bands at angles of 60^o and 120^o with respect to the nanowire growth direction. In the following, we will not comment much more about feature 2, as the physics of amorphization does not depend on the exact nature of this feature.
2. Given the lower resolution of the DFTEM images, in their FFT (**fig. S17d**) we capture information only upto $|k|<1$ nm^{-1} (in reciprocal space, resolution >1 nm in real space). This includes superstructure modulations (feature 3, **fig. S17d)**, emanating out of periodic In and Se vacancy bands perpendicular to the nanowire growth axis. and a halo of diffuse scattering emanating out of disorder in the form of sliding faults (feature 4 in **fig. S17d**). In the following, we will track the changes occurring to the wire using both DFTEM videos and corresponding FFTs. Within the limited resolution that DFTEM offers, we will use superstructure modulations in FFT (feature 3), as a proxy for long-range order in the crystal structure, and reduction in their intensity (and disappearance) along with a simultaneous observation of NDR, followed by collapse in current in the transport measurement will be interpreted as amorphization, consistent with all our ex-situ measurements. As we will see, the long-range order persists until just before amorphization.
3. We also note that carrier wind force, electric field and ensuing piezoelectric stress provide the driving force for the creation of sliding faults, which also couples to polarization rotation locally. We observe that these faults are formed in various regions of the nanowire. In the later stages of biasing, our high resolution HRSTEM imaging shows that creation of sliding faults, their multiplication and interaction eventually lead to the frustration of polarization with several polarization domains (distorted structure(s) as referred to by the referee). each domain having a similar coherence length as a stacking domain (shown in **fig. 3** in the manuscript) Given the nature of all these various defects and their strong coupling, in the following we do not distinguish between stacking domains and ferroelectric domains and address them as domains separated by domain boundaries.

***Description of feature evolution with in-situ biasing*:**

1. **Movie S1** shows that small bias voltages (~5 V) also create subtle dynamics to the already existing sliding defects (as can also be noted from the series of FFTs at different times, **fig. S18 a-d**). While we do not delve into the exact nature of these subtle changes, we note that the FFTs taken from very local regions of the wire where several sliding faults intersect, is devoid of any periodicity (**fig. 4 a-d**), indicating loss of local structure over several regions.
2. **Movie S2** shows the device dynamics upon subjecting to I-V stressing from 15 to 25 V. In the transport behavior, while we see an initial increase in current with voltage (in the order of 10's of microamps), we observe current fluctuations at an applied voltage of ~20 V (when the device current goes beyond 30 μA, **fig. 4e**). This is the same behavior as reported in **fig. 3a** in the manuscript (obtained from another device), where *current fluctuations* (or

local field fluctuations) occur before the NDR. The DFTEM video shows that *concomitant with the current fluctuations (or local field fluctuations), the strain field also fluctuates in a very correlated manner* (snapshots in **fig. 4f-h**).

3. The perfect synchronization between strain field fluctuations and local electric field is evidence of piezoelectricity. In conventional ferroelectrics (which are also piezoelectric), a slowly varying electric field causes domain boundaries to move and interact emitting jerks,[7,8] both in the acoustic domain as well as in the electric domains. Such noise (Barkhausen noise) is well studied and modeled for domain wall motion in disordered medium.[9] Barkhausen noise shows long-range spatiotemporal correlations and follows similar universal physics as that of earthquakes. While, the point of this paper is not to analyze this noise, we note that given that our system also has induced disorder in the form of sliding faults, and domain boundary motion within this disorder, leading to fluctuations (or Barkhausen like noise) in both strain fields (observed from TEM), and local electric fields (observed from transport). Conversely, observation of such noise stands as an evidence of polarization rotation and interaction among domains.[10]
4. To summarize, a combination of semiconducting nature, and ferroelectricity enables both carrier wind, electric field and ensuing piezoelectric stress to provide sufficient driving force for layer sliding, polarization rotation and domain formation. These processes positively feedback into each other creating smaller and smaller domains. Once the density of (stacking) domains and domain boundaries increases such that they are within interaction distance of each other, they interact with each other creating strain field fluctuations.
5. **Movie S3**, the final video, presents the process of amorphization when the device is electrically stressed with a voltage varying slowly (and linearly) between 35 and 45 V. Note that this video was recorded immediately after **Movie S2**. We see that the current in the device starts at ~5 μA (less than the current through the device in Video S2) suggesting that the defect concentration that reduces the carrier mobility has increased, thanks to the positive feedback process described before. An increase in average current with some fluctuations (also strain field fluctuations in DFTEM) is first seen up to a point where the device current reaches ~15 μA, beyond which carrier wind force and electric field provide sufficient driving force for defects (sliding defects, domain boundaries) to interact over a longer range creating larger strain field fluctuations.
6. Upon following the FFT of the DFTEM image, we see that the FFT to start with, shows streaky patterns of what were sharper modulation vectors (in **fig. 4j**), clearly suggesting an increase in disorder (decrease in coherence length) of the In/Se vacancy bands perpendicular to the nanowire. At the point where "large" fluctuations in current begin (at 60 s in **fig. 4i**) these streaky patterns lose intensity in the main modulation peaks becoming more diffuse (in **fig. 4k**). This, we believe, is the onset of disruption of long-range order in terms of In/Se vacancy band periodicity (and also a proxy to the overall crystal structure). These large length scale strain field fluctuations, eventually lead to a collapse of the current

(showing the values measured in amorphous phase, **fig. 4l**), and a complete disappearance of long-range periodicity, with FFT of DFTEM image showing only diffuse scattering (in **fig. 4l**).

7. Based on the *in-situ* TEM data (and our high-resolution STEM images) we propose the following model for amorphization: Electric field and carrier wind force provide driving force for polarization rotation (domain boundary motion) and sliding fault formation, initially in a local region (nanometric). The ensuing piezoelectric stress due to polarization rotation creates similar defects in a longer range, dictated by the length scale of the mechanical stress created by a local sliding fault creation. Once these faults are within interacting distance of each other, they interact causing strain field fluctuations (shocks/ jerks/ Barkhausen noise). The strain field fluctuations (jerks) further create (replicate) more sliding faults, and their ensuing interactions amplified over much longer range (length scale determined by the length scale of acoustic jerks), creating smaller and smaller stacking domains (as observed from HRSTEM image, **fig. 3f** in manuscript). This process continues with positive feedback between stress fluctuations and domain boundary interaction, leading to much smaller domains (and more domain boundaries), which are replicated in much larger regions due to amplified strain field fluctuations and their spatial range. The process keeps continuing and amplifying, and only is restricted by the finite size of the system (length and width of the nanowire).
8. Interaction of various sliding faults at a local scale causes loss of long-range order locally (nanometer scale, **fig. 4d**). Let us consider this as a "nucleation" event of the amorphous phase. The long-range strain fields and fluctuations amplify and replicate this behavior spatially (we observe up to micrometre length scales), and this can be construed as multiple nucleation events of the amorphous phase. All these amorphous nuclei can also locally grow as acoustic jerks also will locally disrupt the crystalline order. Thus, our solid state amorphization process can fall under the purview of nucleation limited phase transition models (which will be explored as a future work). It is interesting to note that although, solid state amorphization was also observed earlier in other chalcogenide systems such as GeTe (metallic) and GST,[11,12] such long range amorphization was absent in those cases owing to them not being piezoelectric/ferroelectric which is essential for converting field fluctuations into long-range strain fluctuations.
9. Finally, electrically, a collapse of current (sudden increase in resistance) occurs once the percolative crystalline pathways are cut off completely by the growing amorphous nuclei. Thus, in the transport behavior, we see a percolative phase transition, whereas structurally local formation of the amorphous phase, and its replication through long-range fields occurs even before the percolation occurs.

Supplementary Note 10: Role of In/ Se vacancies in amorphization: The role of periodic indium and selenium vacancy-rich layers in amorphization can be manifold as discussed below:

i. It is well known in chalcogenide semiconductors (GeTe, Ge-Sb-Te alloys) that vacancies self-dope these materials creating charge carriers[13]. We note that all our tested nanowires show the formation and interaction of the sliding faults at current densities of ~0.01-0.1 MA/cm^2, strongly suggesting the pivotal role of electrical current/carrier wind force in the vdW interlayer sliding, Joule heating and eventual amorphization. In other words, semiconducting nature of In_2Se_3 and its doping aided by vacancies can generate sufficient wind force to create defects, which are exacerbated by coupling to field and polarization rotation.

ii. In/Se vacancy-rich layers assist with faster diffusion kinetics for local atomic rearrangement, making the SSA process much easier.

iii. The vacancies can help to accommodate some of the strain due to the mismatch between various nanoscopic domains, thus decreasing the energy barrier for nucleating such nanoscopic domains, which are precursors for SSA. Considering this, it is very likely that formation of sliding faults and nanoscopic domains/ stacking faults initiates from vacancy rich regions, as pointed out by the referee.

iv. The presence of vacancies can also enhance bond distortions, which can aid in SSA.[14]

Supplementary Figures:

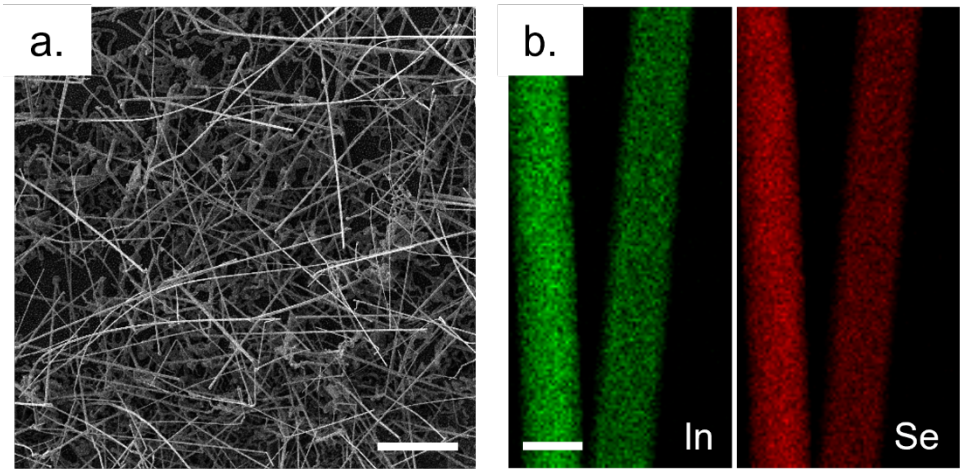

Fig. S1. (**a**) Scanning electron microscopy (SEM) image of a forest of β″-In_2Se_3 nanowires grown on a silicon substrate. (**b**) STEM-EDX mapping of the elements In and Se in two of the as-synthesized β″-In_2Se_3 nanowires. Scale bars: (a) 10 μm and (b) 200 nm.

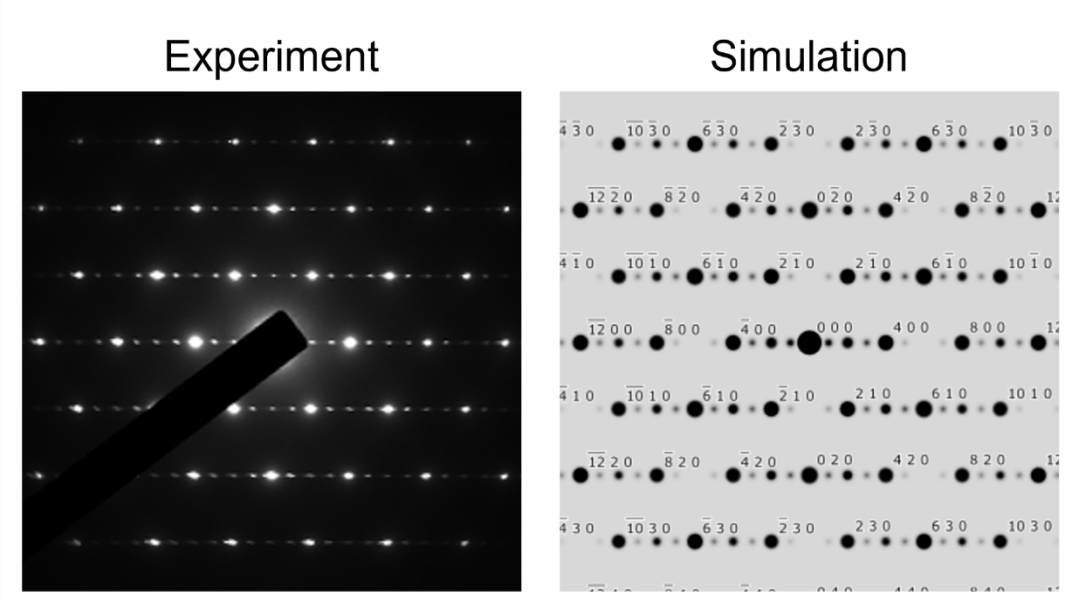

Fig. S2. The experimental and simulated electron diffraction pattern of β″-In_2Se_3 nanowires (generated using CrystalMaker), both showing the presence of three superlattice reflections along the $< 1\ \bar{1}\ 0\ 0 >$ direction.

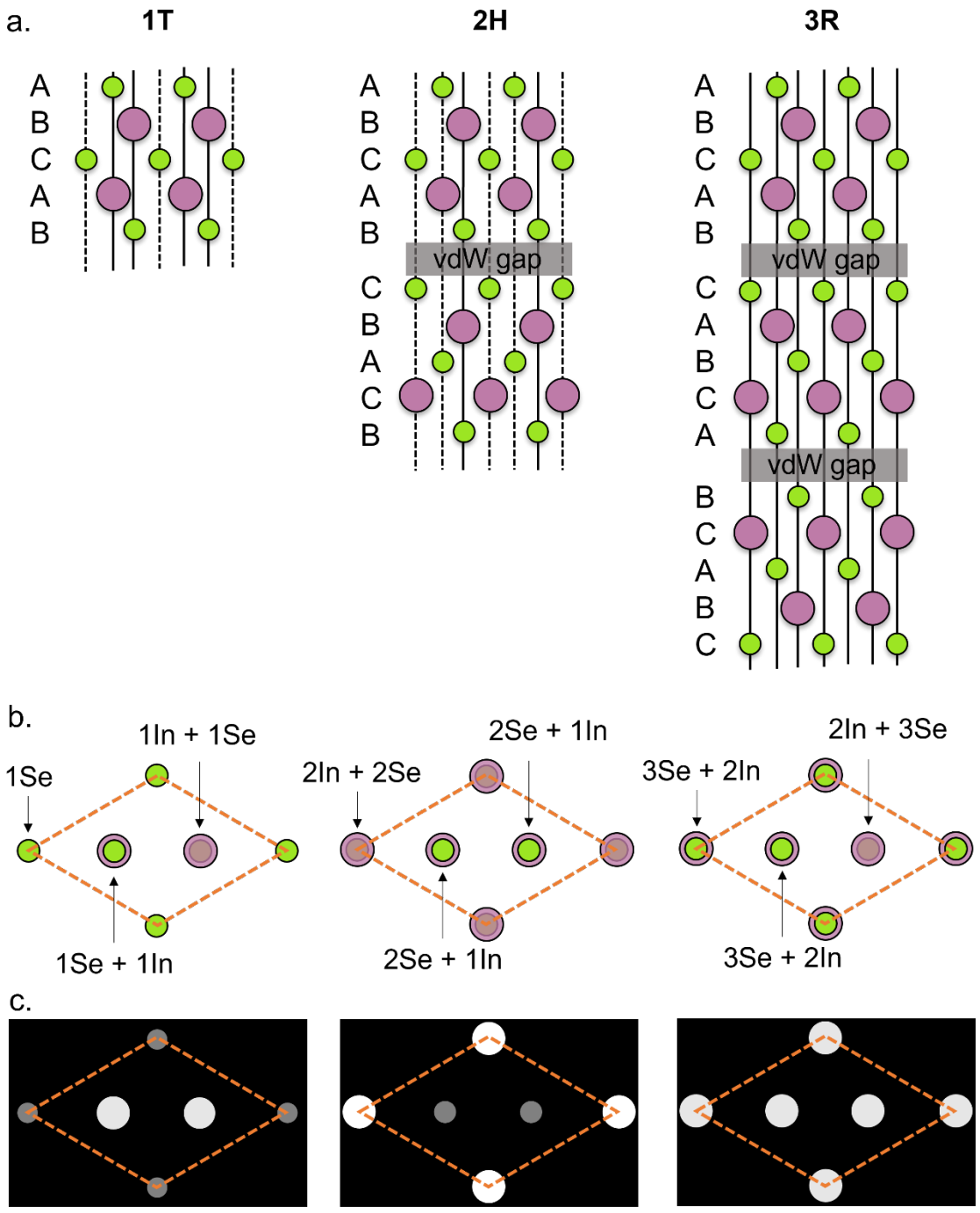

Fig. S3. (**a**) Schematics of the different stacking polymorphs of β-In_2Se_3. Purple and green spheres indicate In and Se atoms, respectively. (**b**) Schematic of the projection of the crystal along the < 0 0 0 1 > zone axis where the black and grey labels indicate the lattice sites visible as bright and dark atoms in the HRSTEM image, respectively. (**c**) Schematic of the STEM images for different stacking configurations of β-In_2Se_3, where the white and gray spheres indicate the bright and dark atoms, respectively in fig. 1b of the main text.

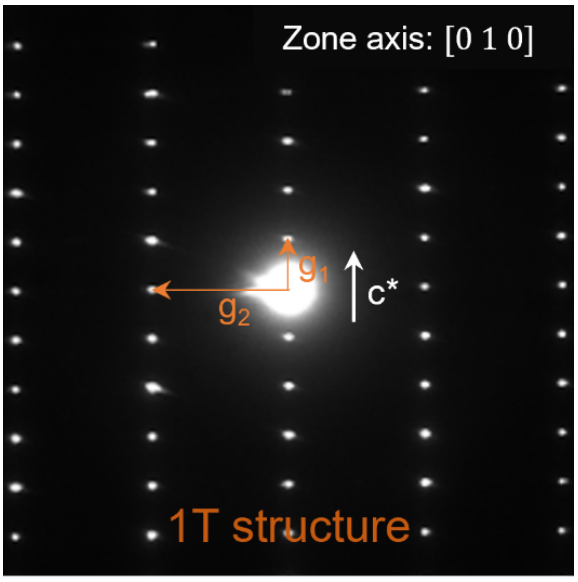

Fig. S4. Electron diffraction pattern of a β″-In_2Se_3 nanowire imaged along the [0 1 0] zone axis, which confirms its 1T stacking configuration. The ratio of the indicated reciprocal lattice vectors is: $^{g_1}/_{g_2} = 0.36$, same as the reported 1T nanowire crystal structure.[15]

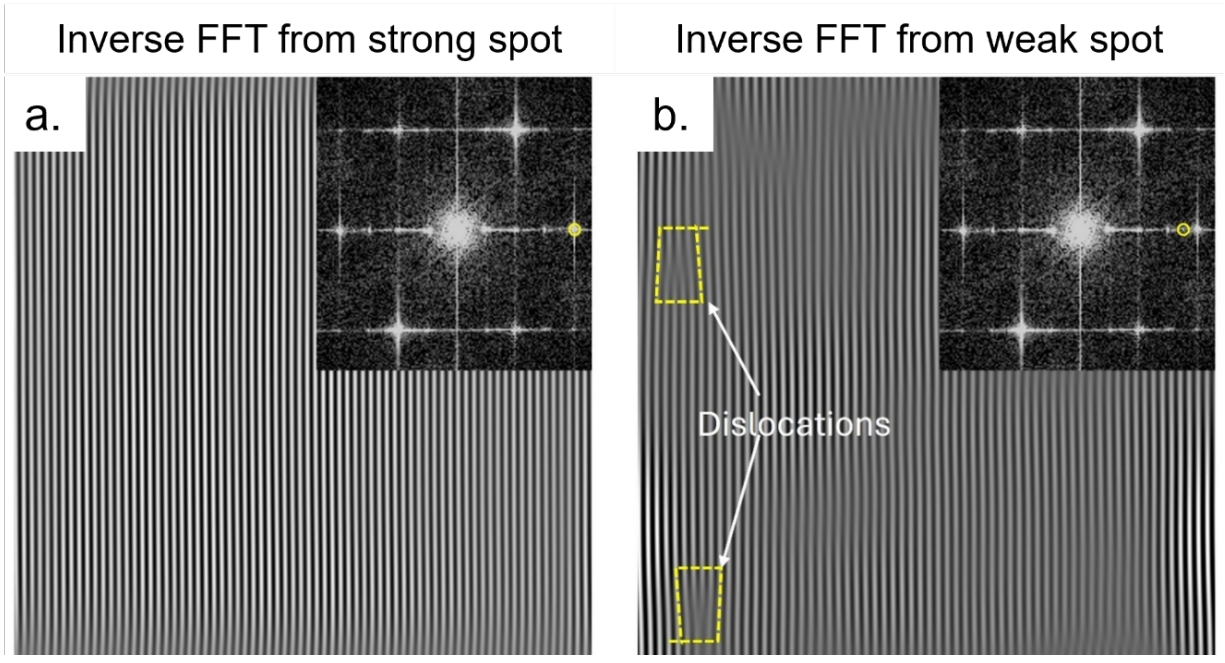

Fig. S5. (**a**) Inverse-FFT (IFFT) obtained from strong and (**b**) weak spot in the FFT of an as-grown β″-In_2Se_3 nanowire (see inset). IFFT obtained from the weak spot shows the presence of dislocations in the nanowire.

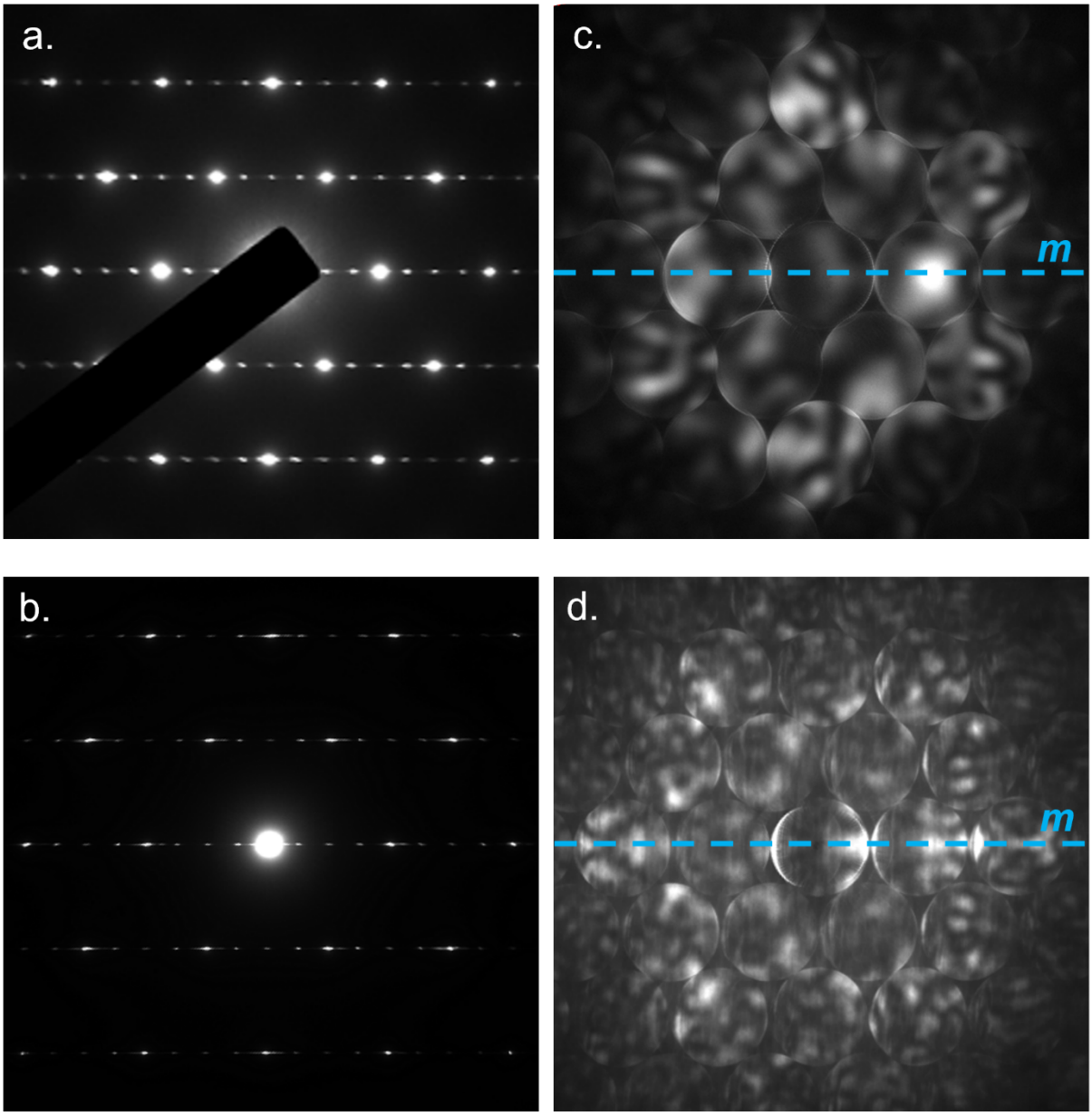

Fig. S6. (**a-b**) Electron diffraction and (**c-d**) the corresponding CBED from two other as-grown β″-In_2Se_3 nanowires showing the presence of a {1 1 $\bar{2}$ 0} mirror plane.

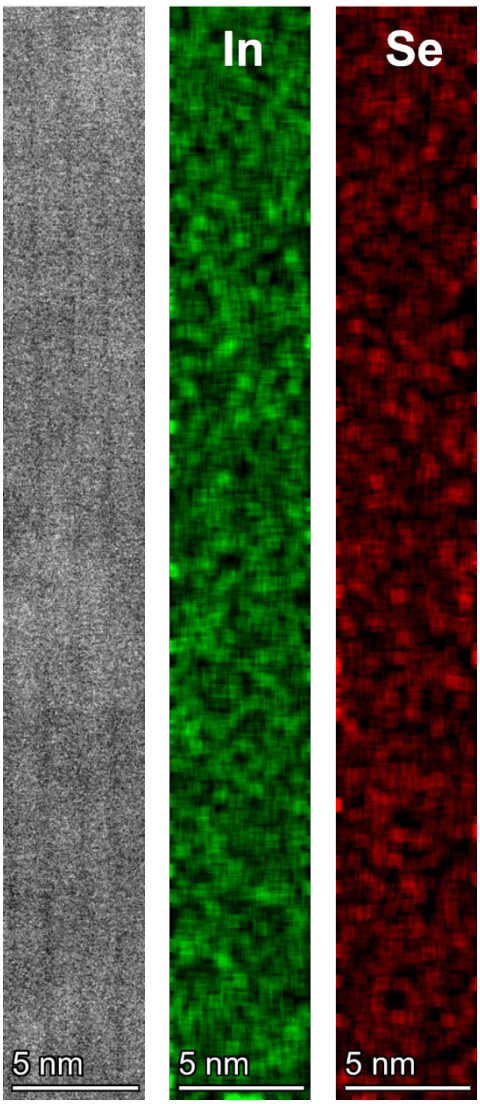

Fig. S7. STEM image of a β"-In_2Se_3 nanowire and the corresponding EDX maps of the nanowires for the elements In and Se. A column-wise average of the elemental composition is shown in fig. 1g of the main text.

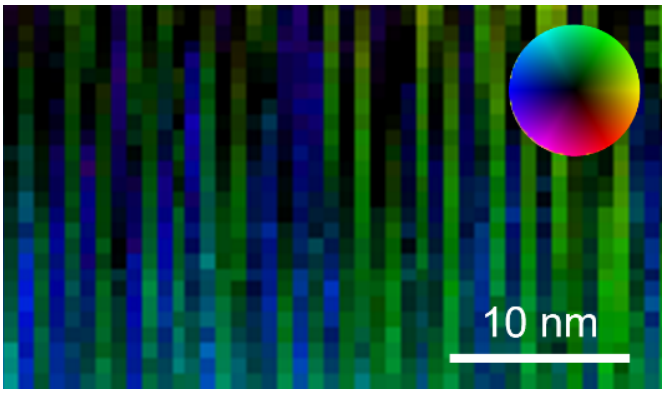

Fig. S8. Four-dimensional STEM mapping[16–18] of electrical polarization for as-synthesized β″-In_2Se_3 nanowire showing that the individual polarization in each nanostripe mainly points along the $< 1\ \bar{1}\ 0\ 0 >$ direction (see color legend) due to displacement of the central Se atoms along this direction.

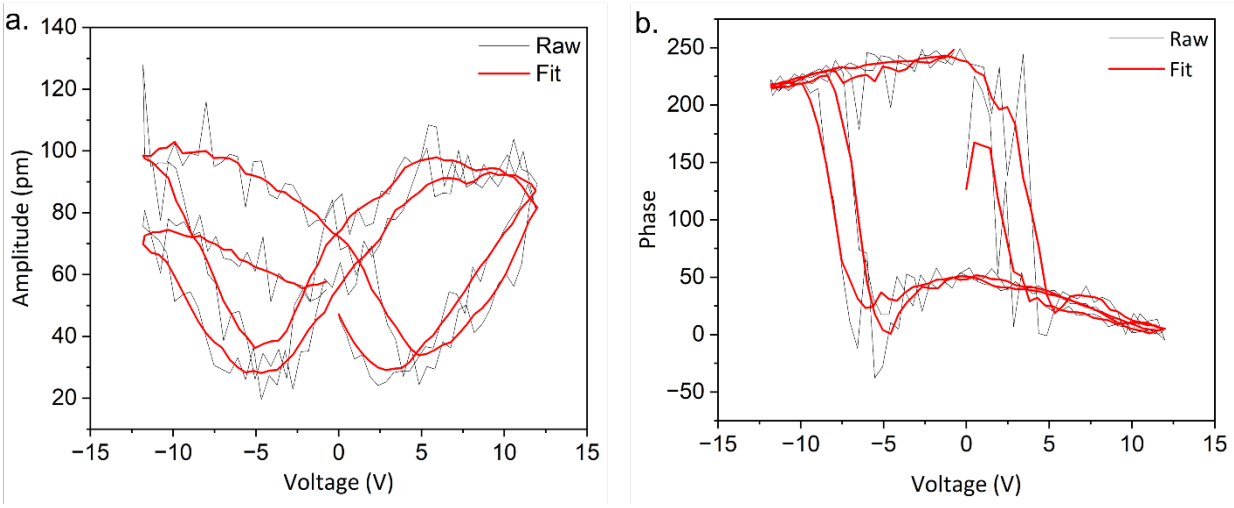

Fig. S9. Piezoforce microscopy (PFM) switching measurements on a β″-In_2Se_3 nanowire showing polarization switching along $< 1\ \bar{1}\ 0\ 0 >$. (**a**) Butterfly-like amplitude response (**b**) Phase response showing a 180° phase flip with electric field.

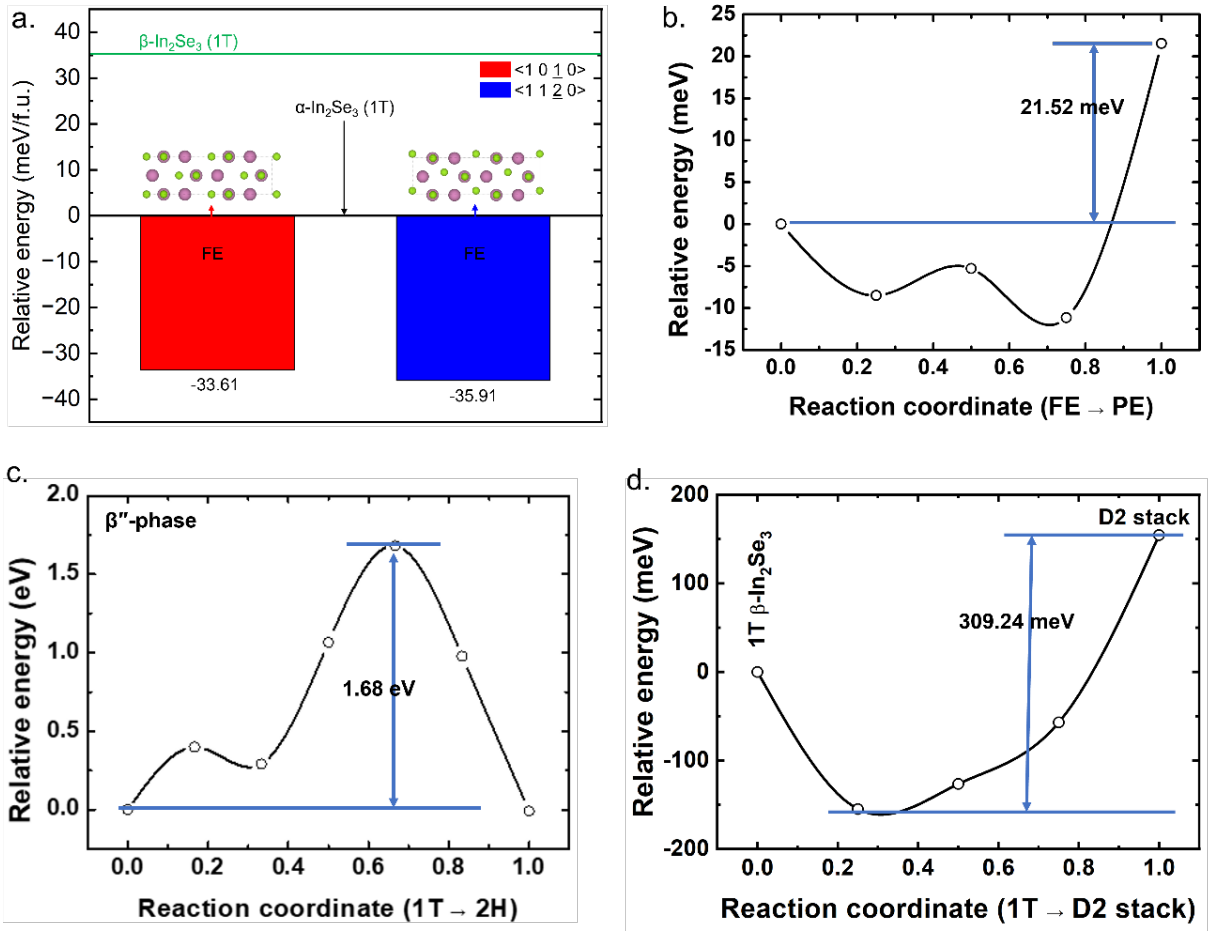

Fig. S10. (**a**) DFT calculations of the relative energies for the $< 1\,\bar{1}\,0\,0 >$ and $< 1\,1\,\bar{2}\,0 >$ direction of Se displacement for the 1T stacking configuration in In_2Se_3 polymorphs. (**b**) Activation energy barrier calculations for transformation from 1T ferroelectric β''- paraelectric β-In_2Se_3 (**c**) transformation from 1T-2H β'' In_2Se_3 and (**d**) transformation from 1T-D2 stacking by interlayer vdW sliding in paraelectric β-In_2Se_3.

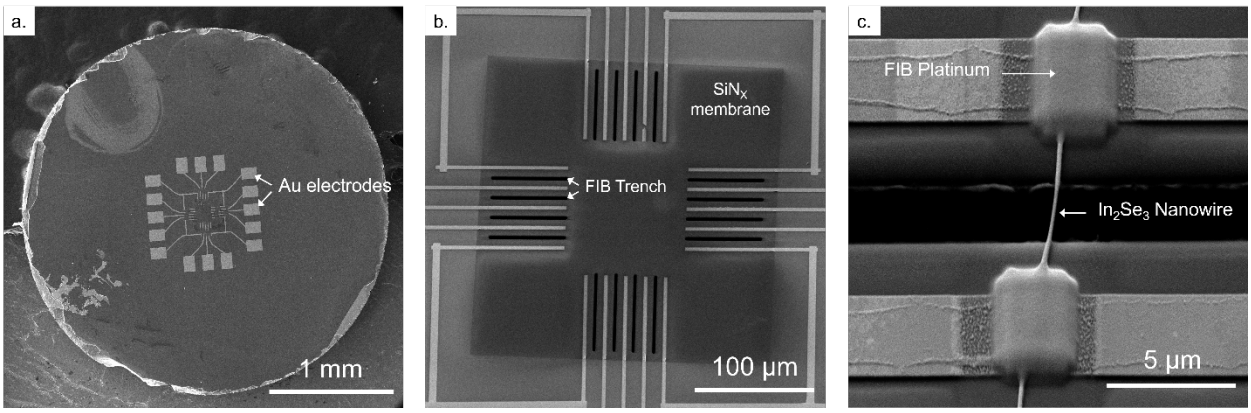

Fig. S11. Scanning electron microscope (SEM) image of a TEM chip for correlating the structure and device properties of β″-In_2Se_3 nanowires. (**a**) Low magnification SEM image of Au electrodes patterned on a Ted Pella TEM grid with a square SiN_x membrane in the center. (**b**) Magnified view of the membrane region of the device depicting the patterned Au electrodes and the trenches made via focused ion beam (FIB). (**c**) High magnification SEM image showing a β″-In_2Se_3 nanowire crossing a trench on which a two-terminal device was fabricated by depositing platinum via FIB.

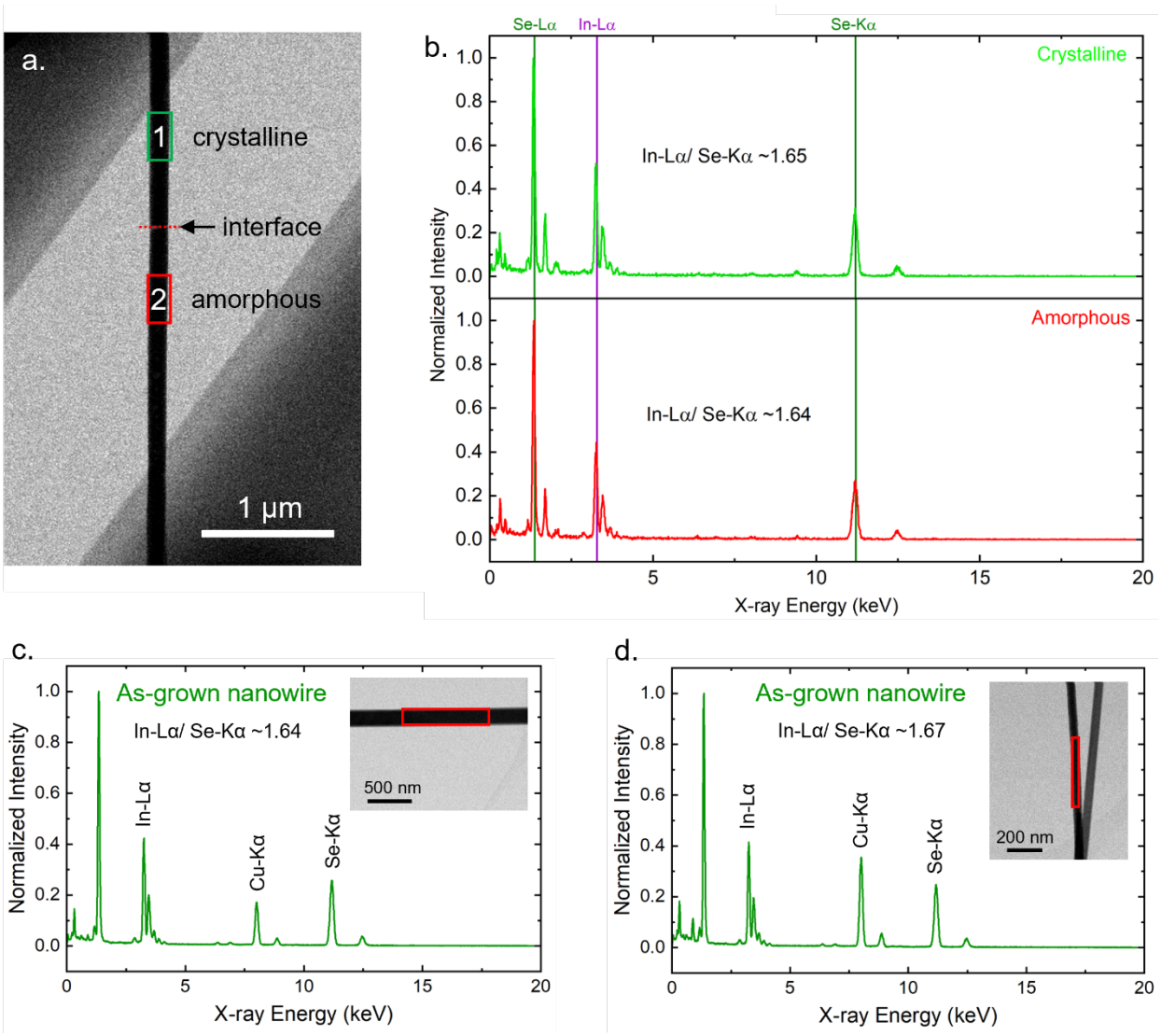

Fig. S12. (**a**) STEM image of the β″-In_2Se_3 nanowire device in fig. 2 of main text after amorphization by d.c. biasing. EDX mapping for the crystalline and amorphous regions are indicated by the green and red boxes, respectively. (**b**) EDX spectrum image indicating that the ratio of In (Lα-peak)/Se (Kα-peak) is similar for the crystalline and amorphous regions of the nanowire. (**c-d**) EDX spectrum for two different as-grown crystalline nanowires showing a similar ratio of In (Lα-peak)/Se (Kα-peak). All the measured as-grown nanowires had this ratio ranging between 1.6-1.7. There is an additional Cu-Kα peak at ~8.04 eV because a Cu based TEM grid was used for these measurements, unlike the SiN/Si based TEM grid in (a-b). Insets depict the STEM images of the nanowires from which the EDS spectrum was acquired.

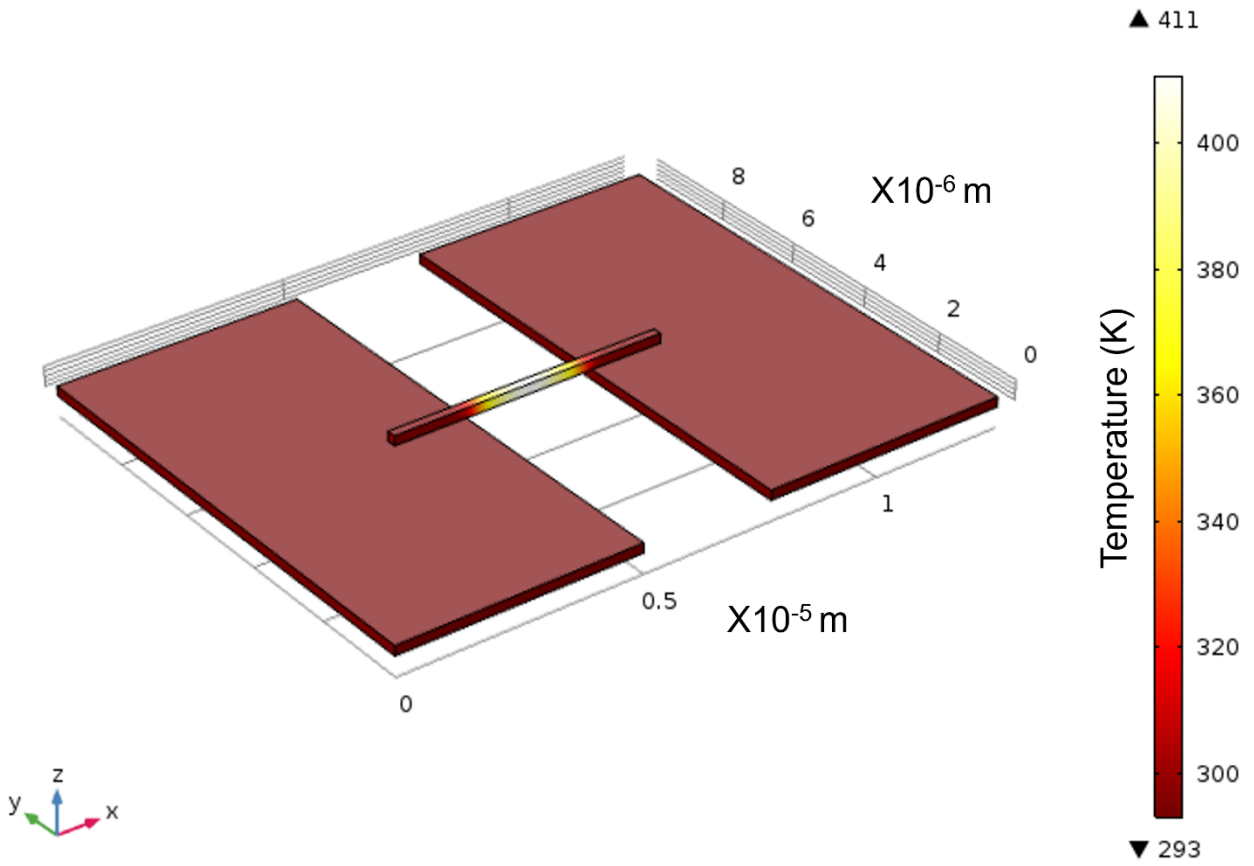

Fig. S13. Finite element COMSOL simulation of the temperature profile in the β″-In_2Se_3 nanowire device shown in fig. 2 of the main text. The simulations were performed under a steady-state approximation when a direct current of 3.5 μA flows in the nanowire. A specific heat C_p of 268 J/(kg.K) and a thermal conductivity κ of 0.3 W/(m.k) for In_2Se_3 were used for the simulations.[19,20] For the boundary conditions, a temperature of 293 K was assumed at the ends of the nanowire and at the bottom of the SiN_X membrane.

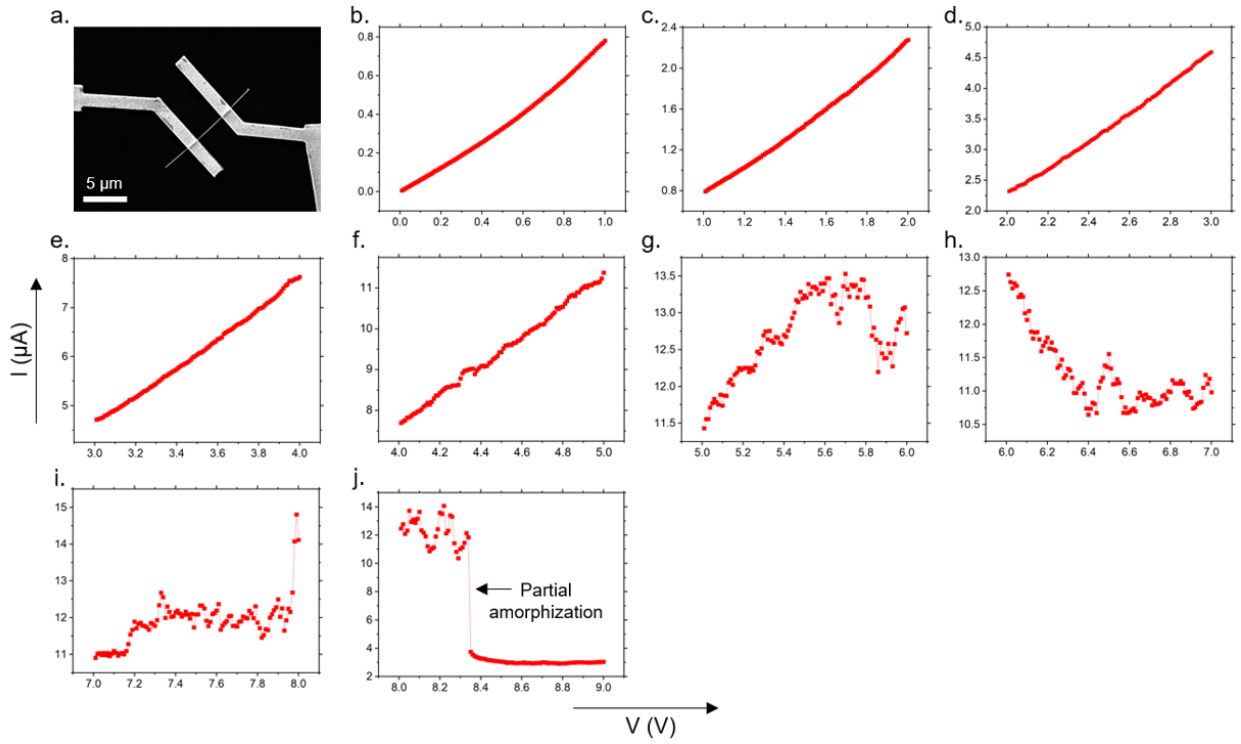

Fig. S14. (**a**) SEM image of a β″-In_2Se_3 nanowire device fabricated via electron beam lithography with Ti/Au electrodes without any FIB Pt deposition. (**b-j**) Similar I-V behaviour of this device compared to the devices on TEM chips. I-V sweeps on the nanowire shows a change in behavior from a positive I-V slope (b-f) to noisy behavior (g), and finally the slope becoming negative (h), indicating an increase in structural disorder (nanowire is still crystalline). Partial amorphization occurs at ~8.35 V (j), indicated by a sudden drop in current.

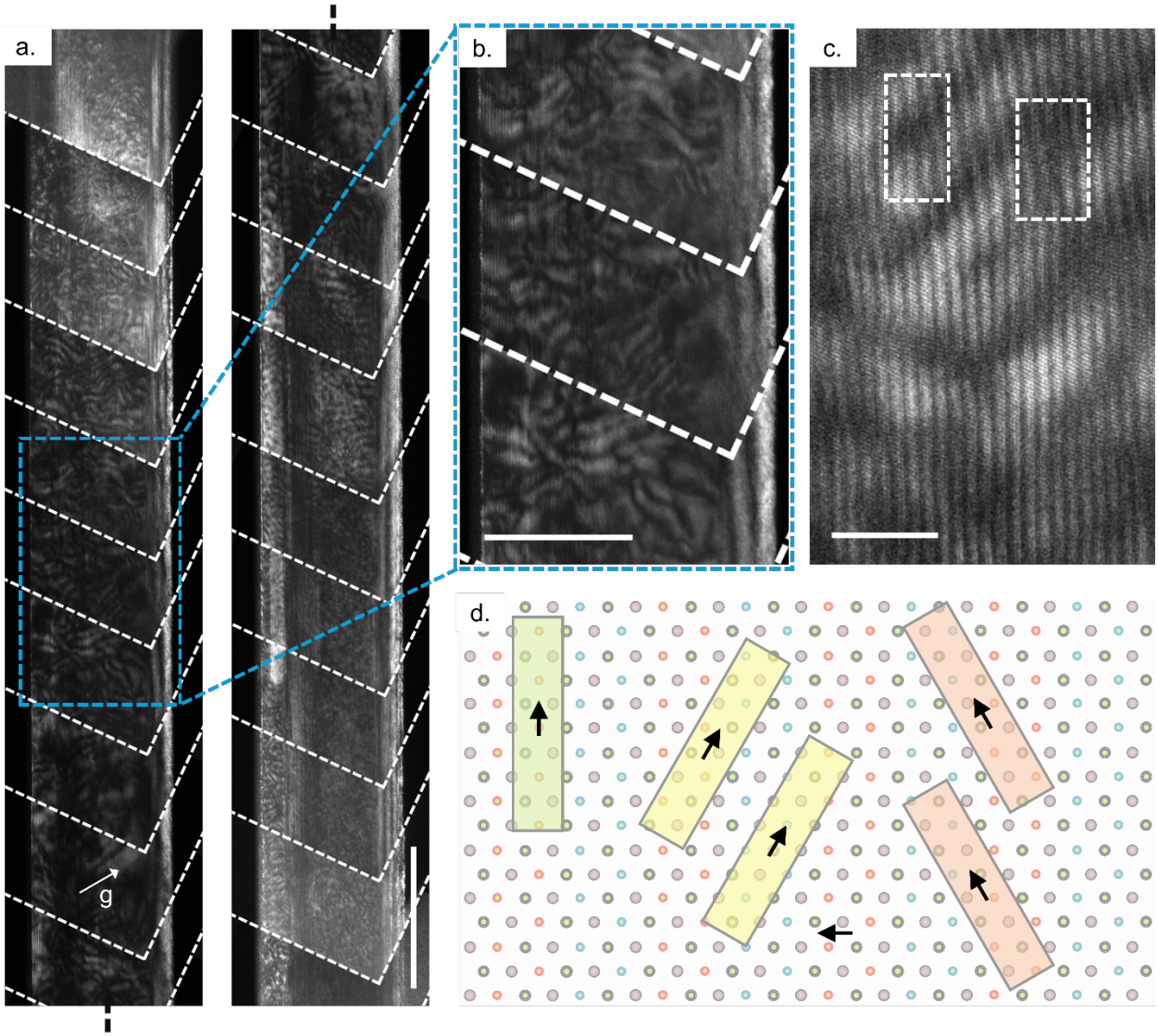

Fig. S15. (**a**) DFTEM images of the β″-In_2Se_3 nanowire device in fig. 3 of the main text after application of multiple I-V sweeps but before amorphization. (**b**) Magnified DF-TEM image from indicated region showing contrast modulation due to overlap of extended defects (stacking and polarization disorder) along the viewing direction. (**c**) High-magnification DF-TEM image clearly showing the presence of numerous sliding faults, some of which are highlighted in white dashed boxes. (**d**) Schematic showing in-plane polarization rotation from initial $< 1\bar{1}00 >$ to $< 11\bar{2}0 >$ and other $< 10\bar{1}0 >$ directions. Nucleation of polarization rotated domains is one of the reasons for the observed contrast in the DFTEM images. Scale bars: (a) 200 nm (b) 100 nm and (c) 10 nm.

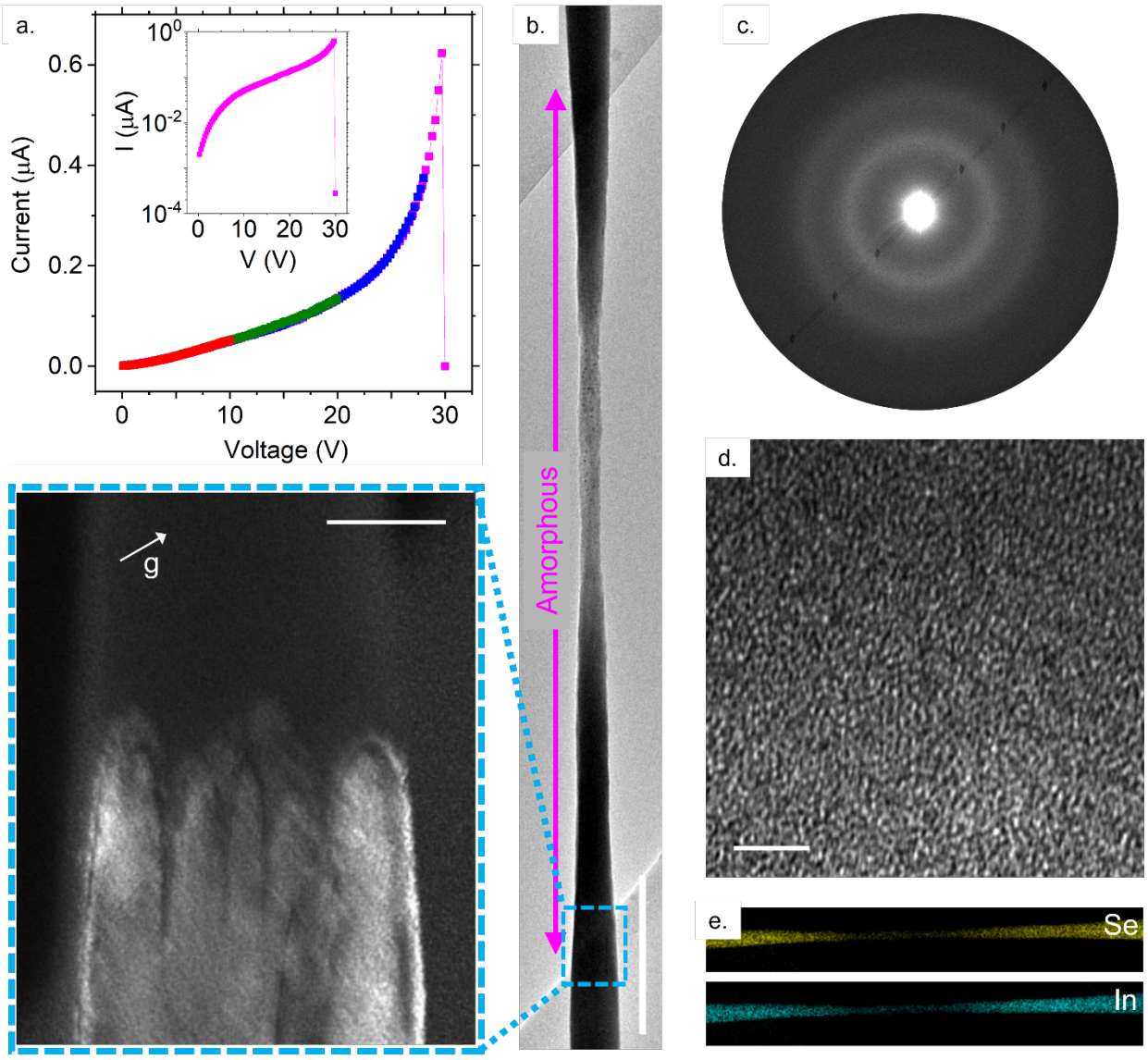

Fig. S16. Amorphization of β″-In_2Se_3 nanowire after applying constant bias to a state with intersecting sliding faults. (**a**) Continued application of a series of d.c. I-V sweeps on the β″-In_2Se_3 nanowire device from **fig. 3** of the main text. At ~30 V, a sudden drop in current is observed. Inset shows the last I-V sweep on a logarithmic scale. (**b**) BF-TEM image of the device showing that almost all the nanowire region suspended on the trench amorphized after the last I-V sweep. Inset in the blue dashed box indicates a DF-TEM image of the crystal amorphous interface. (**c**) SAED of the amorphous region showing the characteristic diffuse halo. (**d**) HRTEM image from the amorphous region. (**e**) EDS signal mapping of the nanowire for the elements In and Se after amorphization. Scale bars: (b) 500 nm, inset in (b) 50 nm, (d) 2 nm.

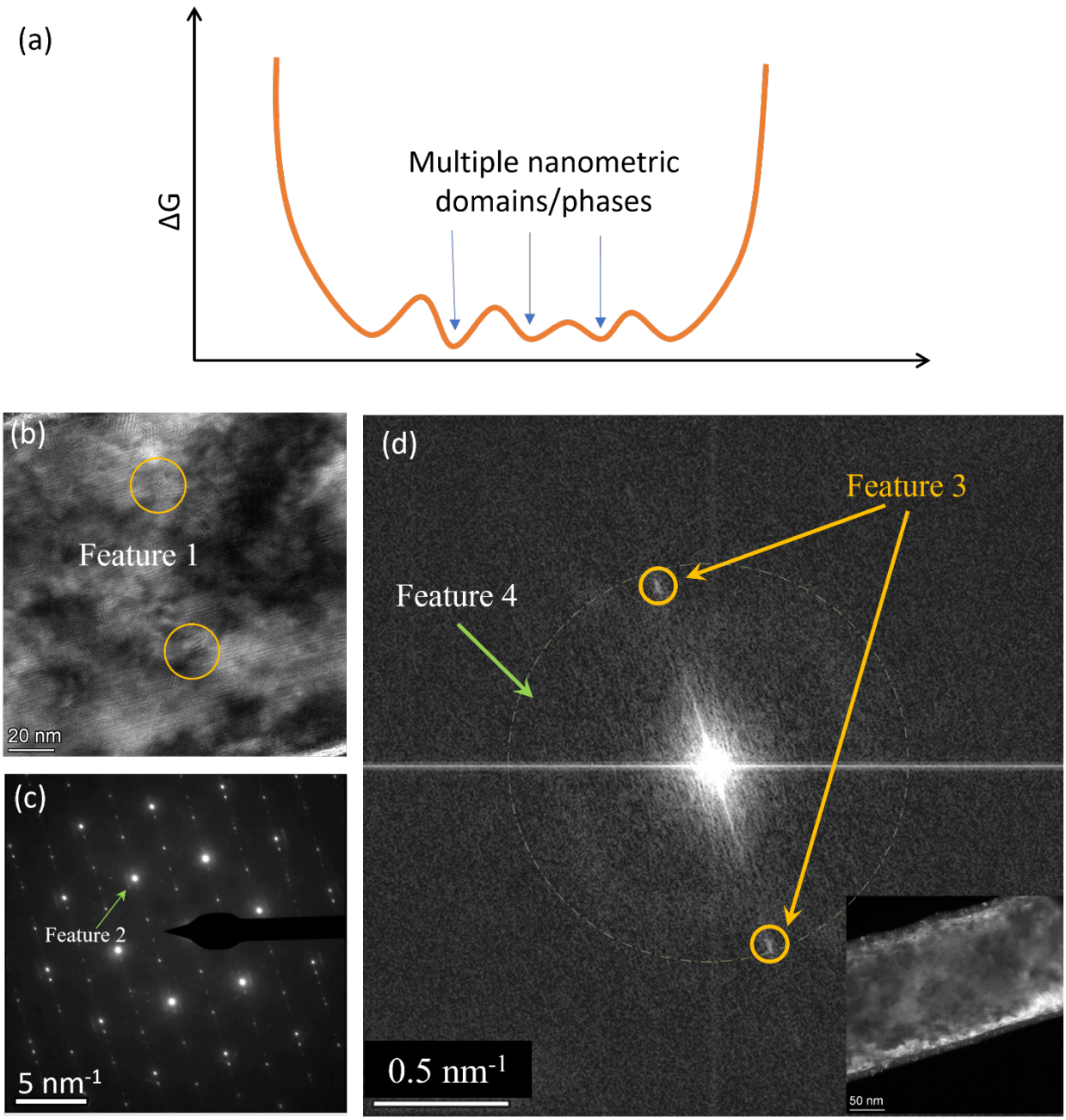

Fig. S17. (a) Schematic of the free energy landscape with multiple minima showing that multiple states are possible, which results in multiple domain formation just before amorphization in d.c. biased β″-In_2Se_3 nanowires (**b**) DFTEM image with Feature 1 highlighted in circle showing sliding faults (**c**) SAED from the same region showing superstructure reflection (marked as feature 2) due to sliding faults creating modulations in well-defined directions (**d**) FFT (from inset in (d)) showing streaks perpendicular to band direction as feature 3 and halo diffuse scattering marked in circle as feature 4.

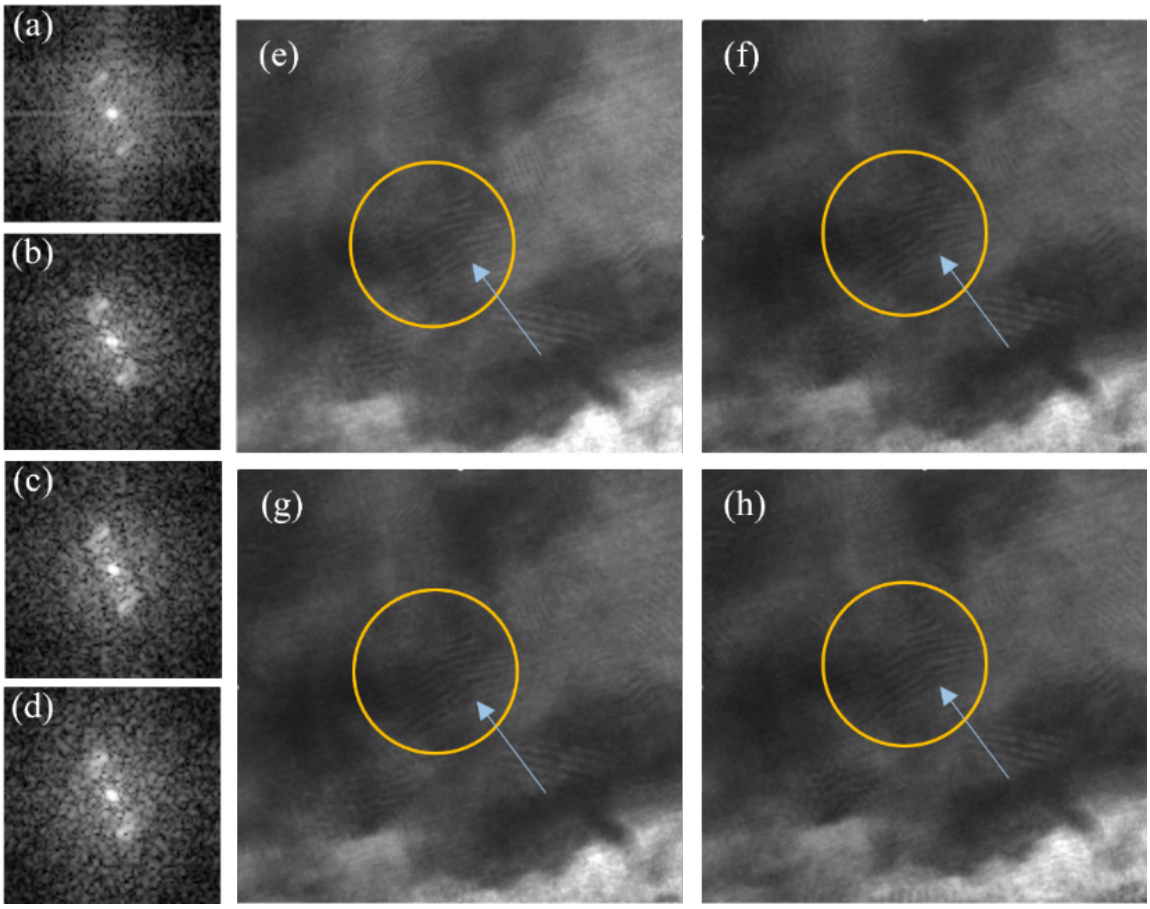

Fig. S18. (**a-d**) Series of FFTs taken at various time frames when biasing at low voltages obtained from the circled regions shown in the corresponding DFTEM snapshots in (e-h). The subtle changes in evolution of the sliding fault can be better observed through FFTs in (a-d).

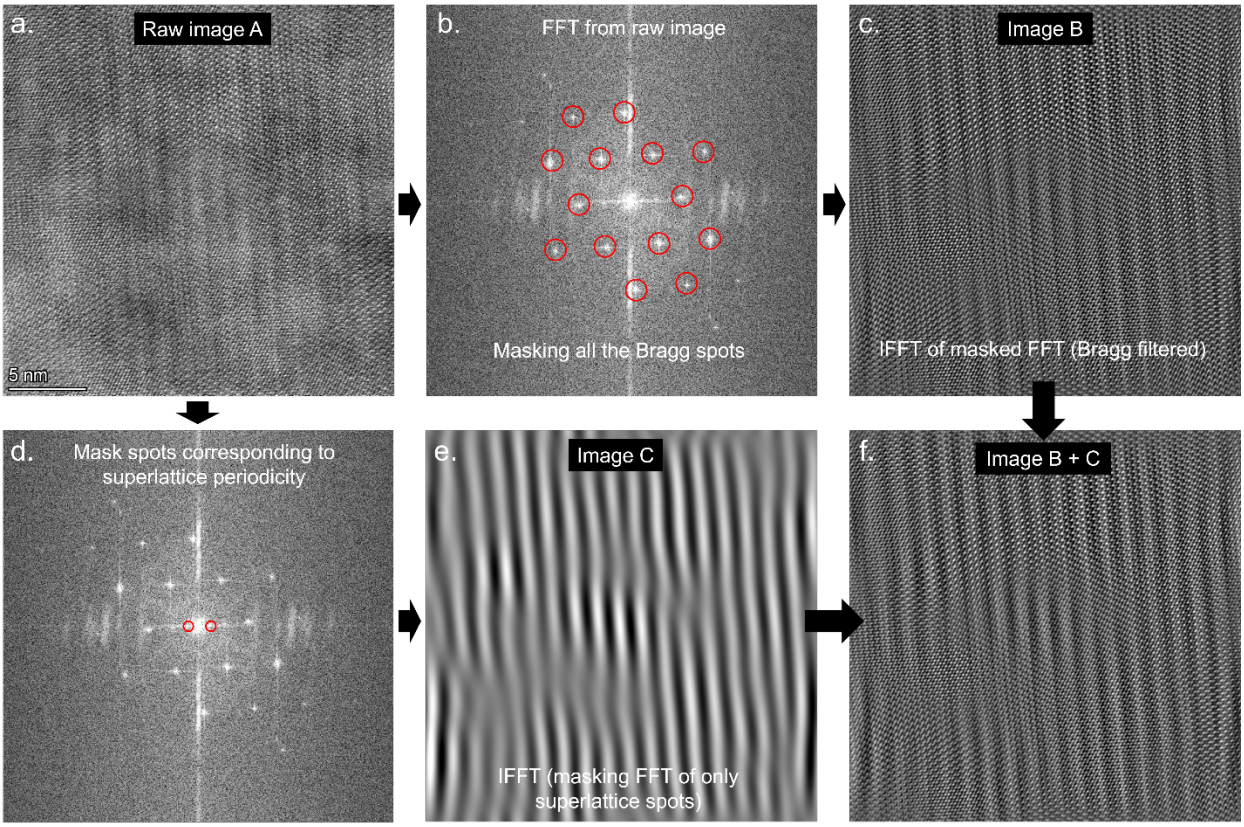

Fig. S19. Image processing method to enhance the contrast of sliding faults in HRSTEM images of d.c. biased β″-In_2Se_3 nanowires. (**a**) Raw HRSTEM image and its (**b**) corresponding FFT. (**c**) Inverse FFT (IFFT) obtained by masking the Bragg spots indicated by red circles in (b). (**d**) FFT showing the masking of superlattice spots which is used to generate the (**e**) corresponding IFFT image. (**f**) Overlay of image B and C, which greatly helps in enhancing the contrast of the sliding faults.

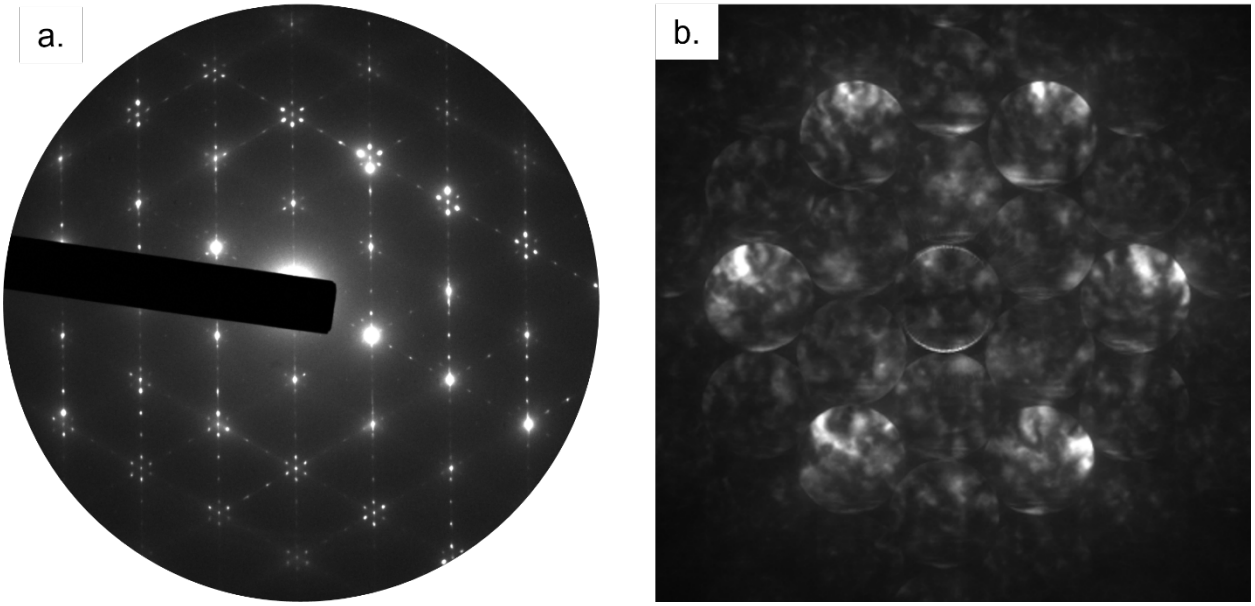

Fig. S20. (**a**) Electron diffraction from a β″-In_2Se_3 nanowire after annealing at 190 ºC for 6 hours under vacuum and argon flow. (**b**) Convergent beam electron diffraction (CBED) from the same nanowire. Although the discs have a six-fold symmetry in this orientation, the higher-order effects within the discs are blurred due to overlapping multiple domains.

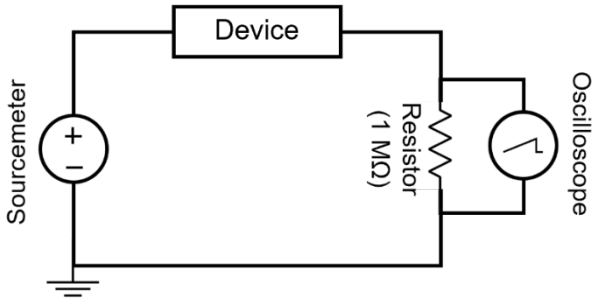

Fig. S21. Schematic of the circuit used for monitoring the evolution of current with time when the d.c. voltage is held constant.

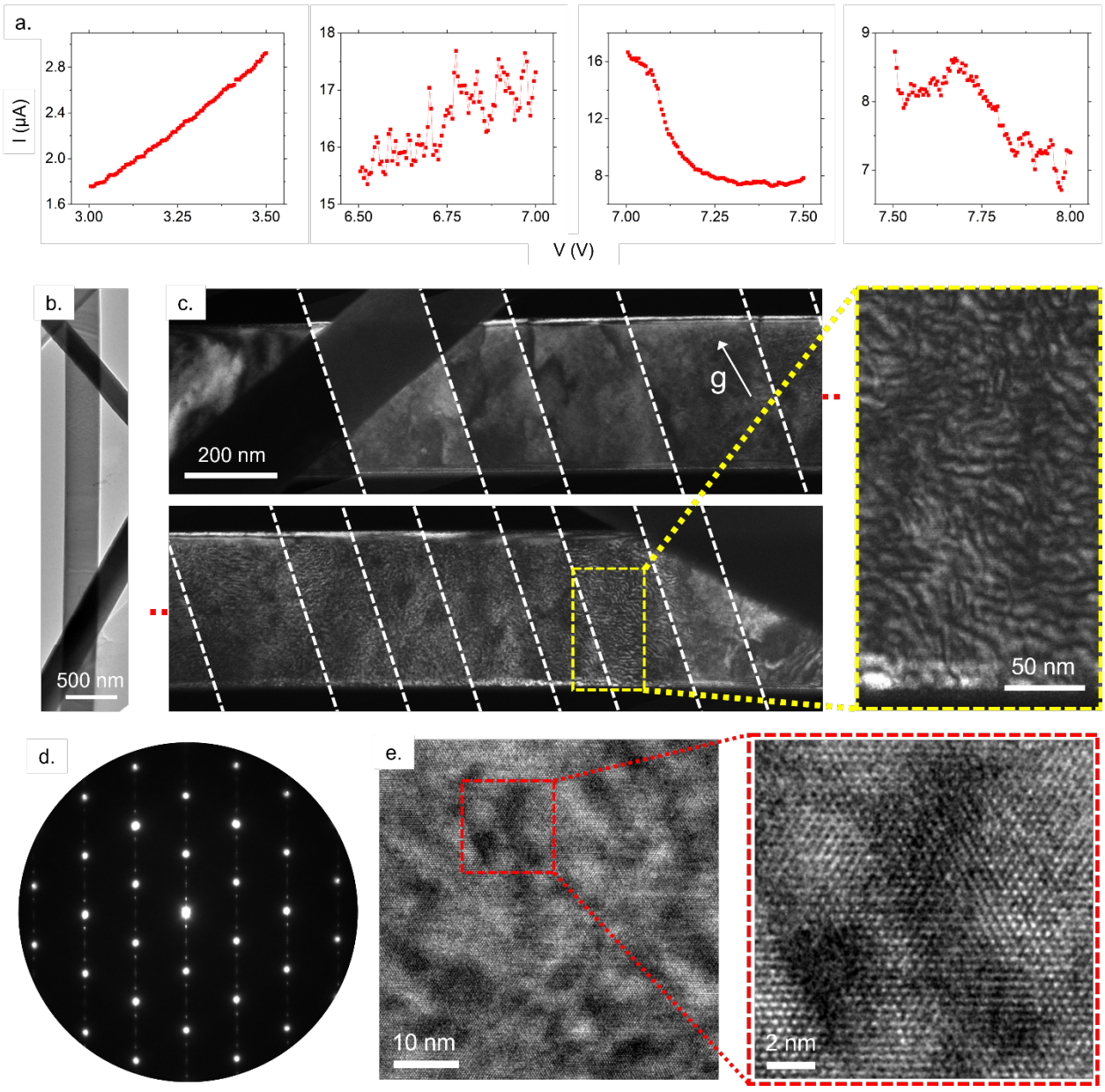

Fig. S22. Electrical and structural characterization of the β″-In_2Se_3 nanowire device when it reaches the negative differential resistance regime (before amorphizing the device). (**a**) I-V sweeps of the nanowire shown in Extended data fig. 1 to estimate the amorphization voltage. There is a change in behavior with increasing d.c. voltage from a positive I-V slope to noisy behavior and finally the slope becoming negative. (**b**) Low magnification BF-TEM of the nanowire device after the initial I-V sweeps. (**c**) DF-TEM image and a magnified region (*inset*) showing contrast modulations due to generation of topological dislocations after the I-V sweeps. (**d**) SAED showing that the three superlattice reflections are still present after the initial I-V sweeps. (**e**) HR-TEM image and magnified region (*inset*) showing the presence of dark contrasts due to defects.

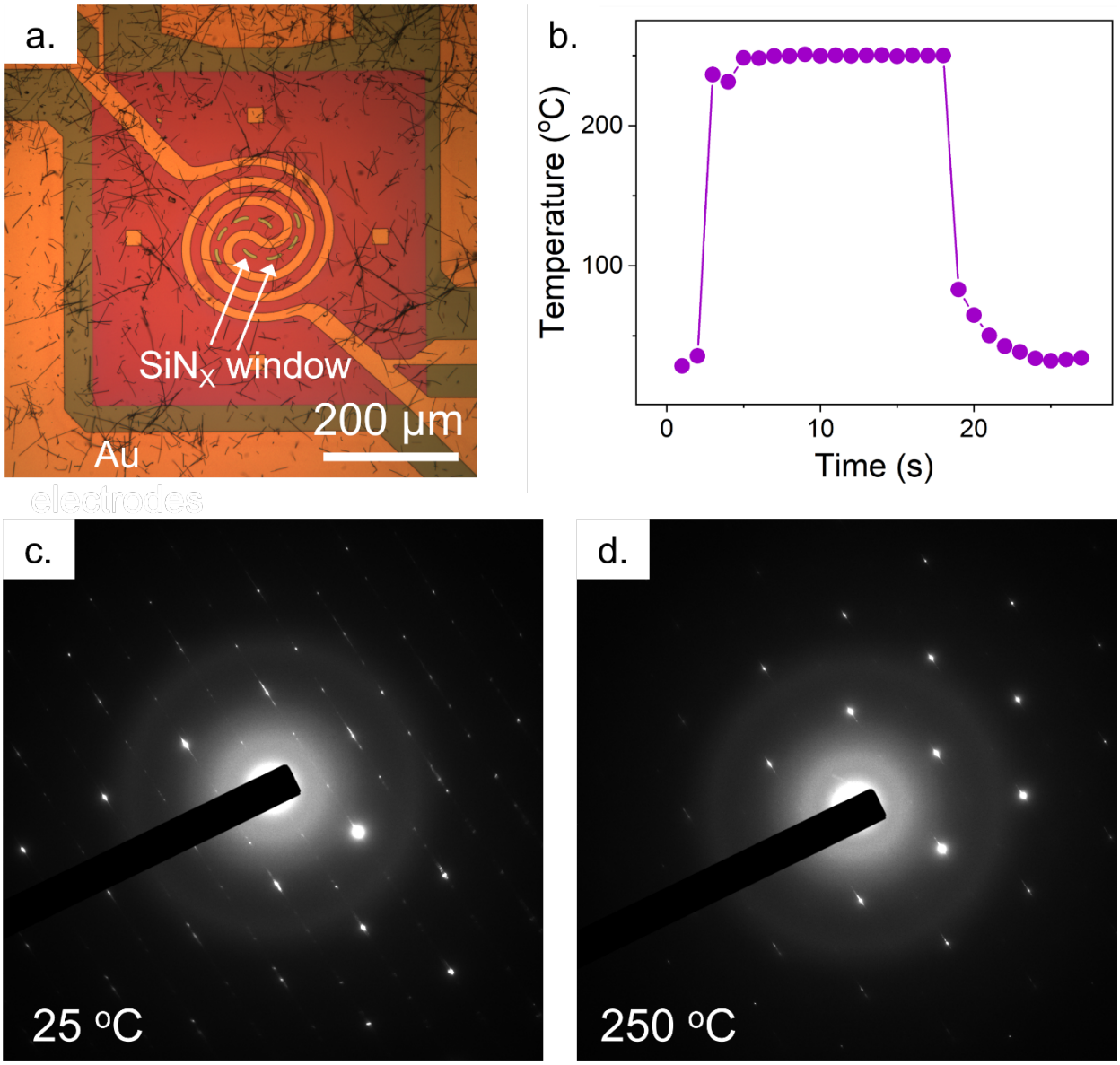

Fig. S23. (**a**) Optical microscope image of a TEM heating chip showing the electron transparent SiN_X viewing window on which the β″-In_2Se_3 nanowires were dry transferred. (**b**) Temperature profile over time during the in-situ TEM heating experiment as is shown in movie S1. The temperature was rapidly increased to 250 °C, held there for 13 s and then rapidly cooled down to room temperature. (**c-d**) SAED of the nanowire captured during the in-situ TEM heating at 25 °C and 250 °C, respectively.

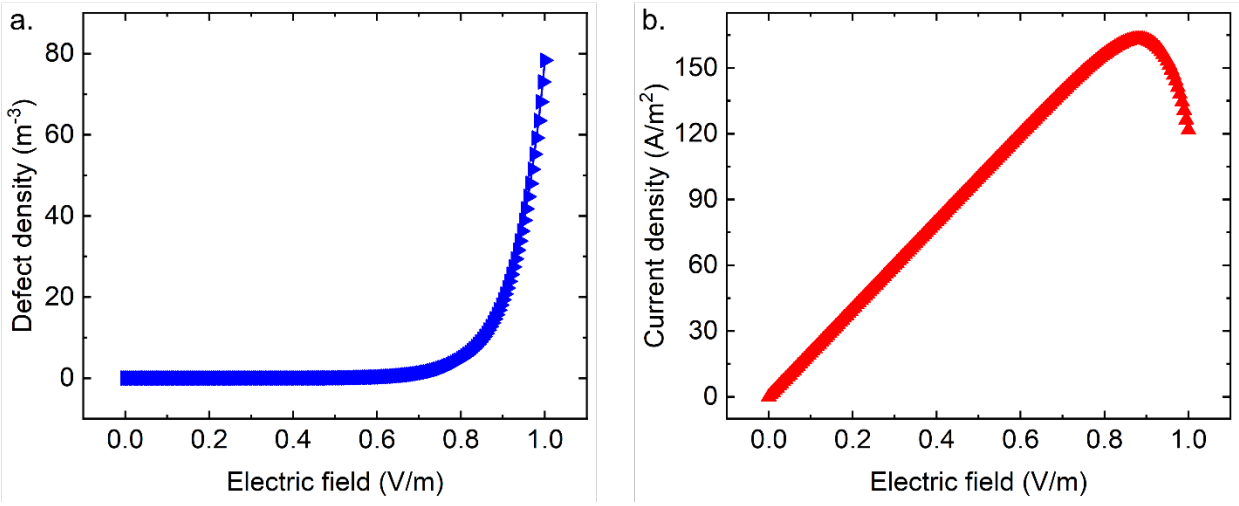

Fig. S24. Theoretically calculated results in β″-In_2Se_3 nanowires for (**a**) defect density as a function of electric field and (**b**) current density as a function of electric field when the d.c. electric field is swept from 0-1 V/m. Negative differential resistance (NDR) behavior is observed for $E > 0.88\ V/m$. These calculations simulate the behavior of devices in fig. 2 and and 3 of main text.

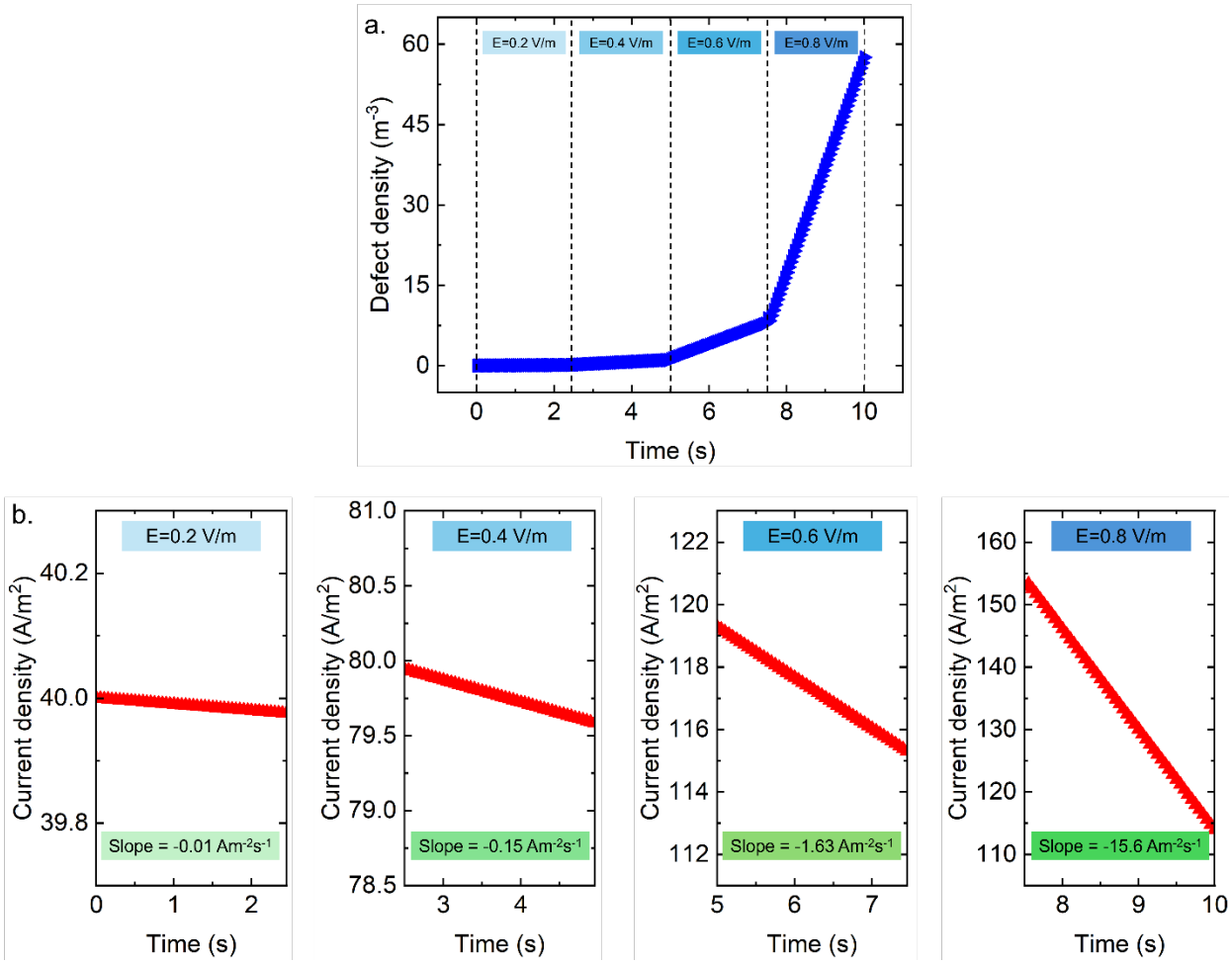

Fig. S25. (**a**) Theoretically simulated defect density and (**b**) current density in β″-In_2Se_3 nanowires for constant d.c. electric field stressing measurements (with stepwise increase) as was performed for the device in Extended data fig. 1. The behavior for temporal evolution of current density is the same as experimental observations. Current density drops more rapidly with time (more negative slope) when the electric field is held constant at a higher magnitude.

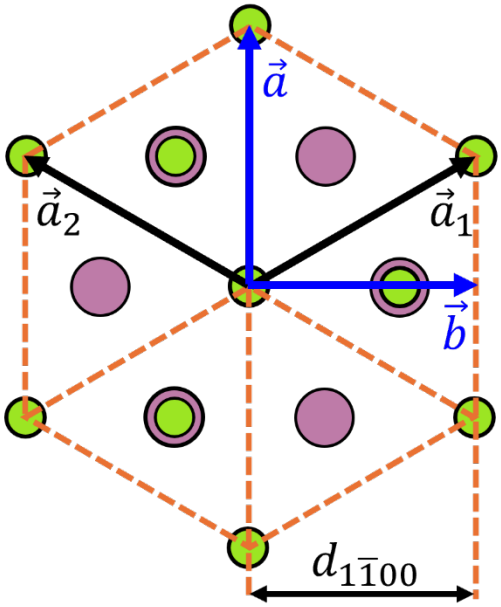

$$\vec{a}_1 = \frac{1}{3}[2\,\bar{1}\,\bar{1}\,0]$$

$$\vec{a}_2 = \frac{1}{3}[\bar{1}\,2\,\bar{1}\,0]$$

$$\vec{a} = \frac{1}{3}[1\,1\,\bar{2}\,0]$$

$$\vec{b} = \frac{1}{2}[1\,\bar{1}\,0\,0]$$

Fig. S26. Schematic showing the coordinate system used to define the unit cell of β″-In_2Se_3 crystal structure and Burgers vector ($\vec{B}$) of the sliding fault (superlattice dislocation) in d.c. biased β″-In_2Se_3 nanowires.

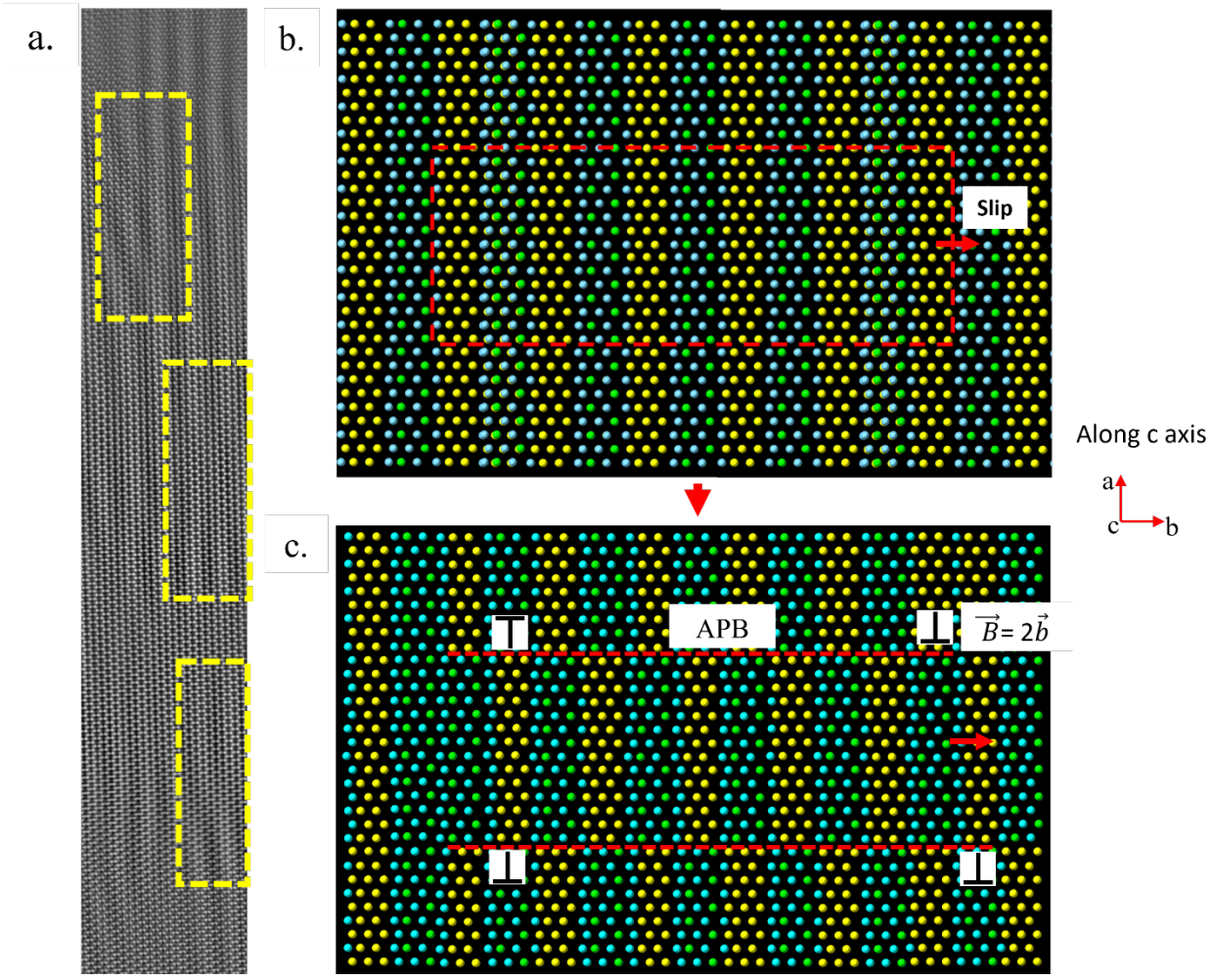

Fig. S27. (**a**) HRSTEM image after biasing a β″-In_2Se_3 nanowire showing sliding faults (superlattice dislocations) generated by sliding one part of the crystal relative to another. The superstructure contrast is enhanced by first Bragg filtering the raw HRSTEM image (**fig. S19c**), and then overlaying it on the Fourier filtered image showing just the superstructure periodicity (as shown in **fig. S19e**) (**b**) shows that the sliding defect can be generated from a slip of a part of the crystal along the vdW layer by $2\vec{b}$ consisting of anti-phase boundary (**c**) (APB, indicated by red dashed lines) and the two partial dislocations with burgers vector ($\vec{B} = 2\,\vec{b}$)

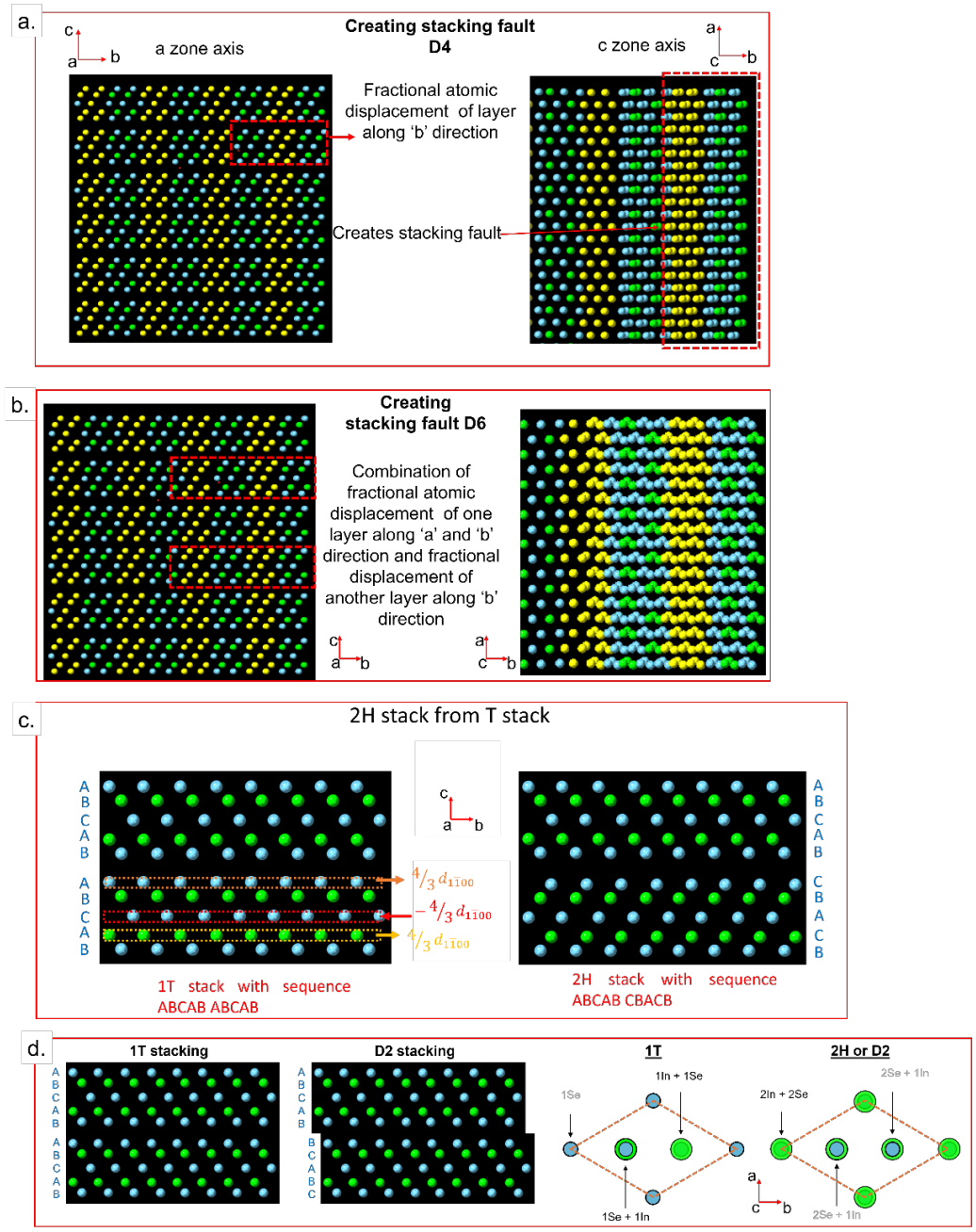

Fig. S28. (**a**) Results from the simulation on steps involved in forming other nanoscopic regions in d.c. biased β″-In_2Se_3 nanowires such as D4 and (**b**) D6. (**c**) Schematic of transformation from 1T (ABCAB ABCAB) to 2H (ABCAB CBACB) structure through slip mechanism. (**d**) Schematic of transformation from 1T (ABCAB ABCAB) to D2 configuration (ABCAB BCABC) through interlayer vdW sliding along $< 1\ \bar{1}\ 0\ 0 >$. Bottom panel shows schematic of projection of crystal along the $< 0\ 0\ 0\ 1 >$ zone axis for 1T and 2H/ D2 stacking configurations showing the mechanism of atom contrast inversion in the HRSTEM image. Lattice sites labeled in black and gray color translate as bright and dark atoms in HRSTEM image, respectively.

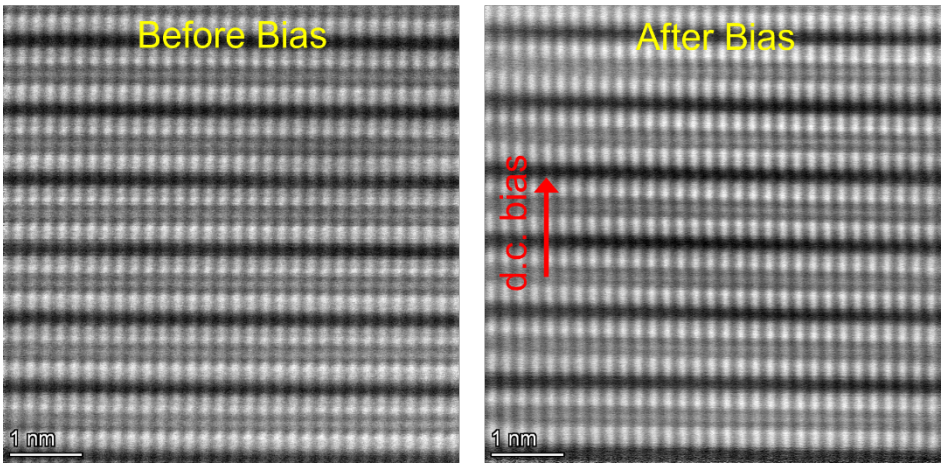

Fig. S29. HAADF-STEM images of d.c. biasing on β″-In_2Se_3 nanowires grown along the '$\vec{c}$' axis do not show any structural changes.

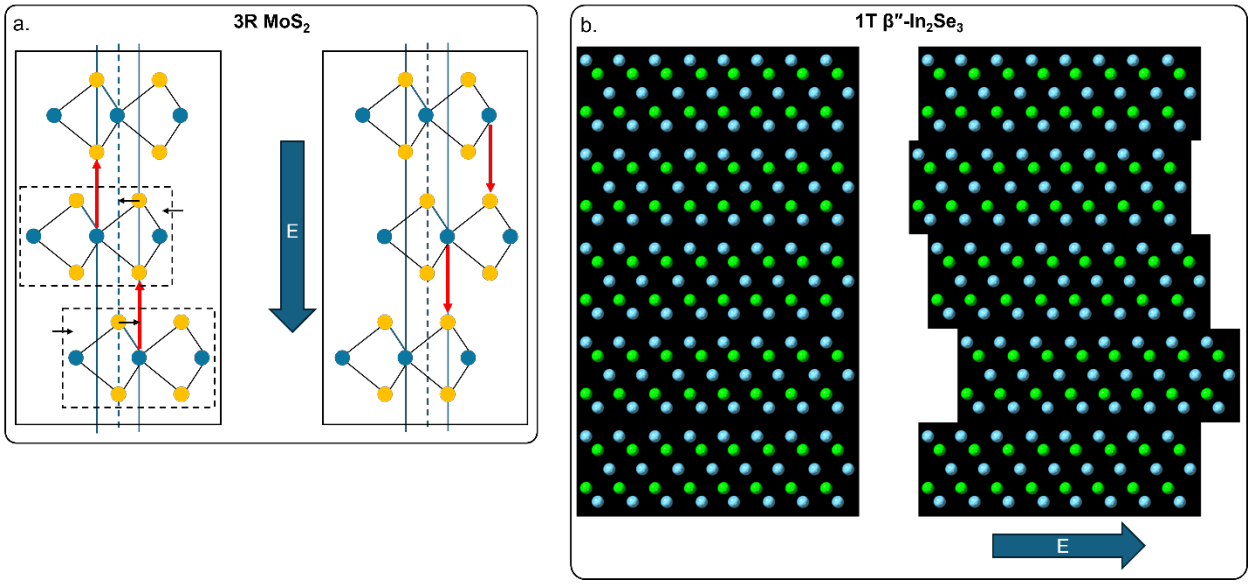

Fig. S30. (**a**) Schematic crystal structure of a sliding ferroelectric 3R-MoS_2, which undergoes polarization reversal by interlayer sliding when a vertical electric field is applied. The coordinated lateral relative movement between the vdW layers causes an interfacial charge transfer resulting in ferroelectric switching, which is very different from the ion displacement mediated switching in conventional ferroelectrics. (**b**) Schematic showing the carrier wind force driven relative interlayer sliding between different vdW layers when a horizontal electric field is applied to β″-In_2Se_3. The uncoordinated slipping between different layers results in loss of interlayer registry and the resulting defective structure helps in solid-state amorphization.

Caption for Supplementary Movies:

Movie S1. DFTEM in-situ biasing movie of β″-In_2Se_3 nanowire device showing subtle evolution of structure at low d.c. biasing voltages (≤5V). Inset shows the magnified region from the region indicated in yellow circle.

Movie S2. DFTEM in-situ biasing movie of β″-In_2Se_3 nanowire device showing structure evolution at intermediate d.c. biasing voltages (15-25 V). The DFTEM imaging contrast, which originates due to strain fields from interacting domains, fluctuates concomitantly with the current (or local field) fluctuations. Inset shows the corresponding current-voltage-time (I-V-t) plot.

Movie S3. DFTEM in-situ biasing movie of β″-In_2Se_3 nanowire device showing d.c. biasing induced amorphization immediately following the current fluctuations observed in Movie S2. Inset shows the corresponding current-voltage-time (I-V-t) plot.

Movie S4. The evolution of selected area electron diffraction (SAED) of a β″-In_2Se_3 nanowire with temperature during the in-situ TEM heating experiment (also see **fig. S23**). The temperature profile over time is shown in **fig. S23b**. The superlattice reflections disappear at 250 ^oC ($T>T_{Curie}$) due to the β″ – β phase transition but reappear on cooling due to β – β″ transition.

Supplementary references:

1. Xu, C. *et al.* Two-dimensional ferroelasticity in van der Waals β'-In2Se3. *Nat. Commun.* **12**, 1–9 (2021).
2. Zhang, F. *et al.* Atomic-Scale Observation of Reversible Thermally Driven Phase Transformation in 2D In2Se3. *ACS Nano* **13**, 8004–8011 (2019).
3. Chen, Z. *et al.* Atomic Imaging of Electrically Switchable Striped Domains in β′-In2Se3. *Adv. Sci.* **8**, 1–8 (2021).
4. Tanaka, M. & Tsuda, K. Convergent-beam electron diffraction. *J. Electron Microsc. (Tokyo).* **60**, 245–267 (2011).
5. Xu, C. *et al.* Two-Dimensional Antiferroelectricity in Nanostripe-Ordered In2Se3. *Phys. Rev. Lett.* **125**, 47601 (2020).
6. Wu, M. & Li, J. Sliding ferroelectricity in 2D van der Waals materials: Related physics and future opportunities. *Proc. Natl. Acad. Sci. U. S. A.* **118**, e2115703118 (2021).
7. Salje, E. K. H., Wang, X., Ding, X. & Scott, J. F. Ultrafast Switching in Avalanche-Driven Ferroelectrics by Supersonic Kink Movements. *Adv. Funct. Mater.* **27**, 1–6 (2017).
8. Casals, B., Nataf, G. F. & Salje, E. K. H. Avalanche criticality during ferroelectric/ferroelastic switching. *Nat. Commun.* **12**, 1–7 (2021).
9. Stefano Zapperi et al. Dynamics of a ferromagnetic domain wall: Avalanches, depinning transition, and the Barkhausen effect. *Phys. Rev. B* **58**, 6353–6366 (1998).

10. Sui, F. *et al.* Atomic-level polarization reversal in sliding ferroelectric semiconductors. *Nat. Commun.* **15**, (2024).

11. Nam, S.-W. *et al.* Electrical Wind Force-Driven and Dislocation-Templated Amorphization in Phase-Change Nanowires. *Science (80-.).* **336**, 1561–1566 (2012).

12. Nukala, P. *et al.* Inverting polar domains via electrical pulsing in metallic germanium telluride. *Nat. Commun.* **8**, 15033 (2017).

13. Edwards, A. H. *et al.* Electronic structure of intrinsic defects in crystalline germanium telluride. *Phys. Rev. B* **73**, 045210 (2006).

14. Kolobov, A. V, Krbal, M., Fons, P., Tominaga, J. & Uruga, T. Distortion-triggered loss of long-range order in solids with bonding energy hierarchy. *Nat. Chem.* | **3**, (2011).

15. Liu, L. *et al.* Atomically Resolving Polymorphs and Crystal Structures of In2Se3. *Chem. Mater.* **31**, 10143–10149 (2019).

16. Ophus, C. Four-Dimensional Scanning Transmission Electron Microscopy (4D-STEM): From Scanning Nanodiffraction to Ptychography and Beyond. *Microsc. Microanal.* **25**, 563–582 (2019).

17. Hachtel, J. A., Idrobo, J. C. & Chi, M. Sub-Ångstrom electric field measurements on a universal detector in a scanning transmission electron microscope. *Adv. Struct. Chem. Imaging* **4**, 1–10 (2018).

18. Zhang, X., Stach, E. A., Meng, W. J. & Meng, A. C. Nanoscale compositional segregation in epitaxial AlScN on Si (111). *Nanoscale Horizons* (2023). doi:10.1039/D2NH00567K

19. Boehnke, U. C., Kühn, G., Berezovski, G. A. & Spassov, T. Some aspects of the thermal behaviour of In2Se3. *J. Therm. Anal.* **32**, 115–120 (1987).

20. Hsin, C. L., Huang, J. H., Spiewak, P., Ciupiński, Ł. & Lee, S. W. Anisotropy of thermal conductivity in In2Se3 nanostructures. *Appl. Surf. Sci.* **494**, 867–870 (2019).